On Mobilization of Lead and Arsenic in Groundwater in Response to CO_2 Leakage from Deep Geological Storage

Liange Zheng[a*], John A. Apps[a], Yingqi Zhang[a], Tianfu Xu[a], Jens T. Birkholzer[a]

[a]Earth Sciences Division, Lawrence Berkeley National Laboratory, 1 Cyclotron Rd, Mail Stop 90-1116, Berkeley, CA, USA

[*]Corresponding author: Tel: 1 510 486 5502, Fax: 1 510 486 5686, email: lzheng@lbl.gov (Liange Zheng)

Abstract

If carbon dioxide stored in deep saline aquifers were to leak into an overlying aquifer containing potable groundwater, the intruding CO_2 would change the geochemical conditions and cause secondary effects mainly induced by changes in pH In particular, hazardous trace elements such as lead and arsenic, which are present in the aquifer host rock, could be mobilized. In an effort to evaluate the potential risks to potable water quality, reactive transport simulations were conducted to evaluate to what extent and mechanisms through which lead and arsenic might be mobilized by intrusion of CO_2. An earlier geochemical evaluation of more than 38,000 groundwater quality analyses from aquifers throughout the United States and an associated literature review provided the basis for setting up a reactive transport model and examining its sensitivity to model variation. The evaluation included identification of potential mineral hosts containing hazardous trace elements, characterization of the modal bulk mineralogy for an arenaceous aquifer, and augmentation of the required thermodynamic data. The reactive transport simulations suggest that CO_2 ingress into a shallow aquifer can mobilize significant lead and arsenic, contaminating the groundwater near the location of intrusion and further downstream. Although substantial increases in aqueous concentrations are

predicted compared to the background values, the maximum permitted concentration for arsenic in drinking water was exceeded in only a few cases, whereas that for lead was never exceeded.

Keywords: CO_2 sequestration; Lead; Arsenic; Reactive transport; Numerical simulation, Groundwater quality

1. Introduction

One promising approach to mitigate the impact of increasing gas atmospheric CO_2 is to capture this gas from stationary generators and inject it into deep geologic formations (Bachu, 2000; White et al., 2005). With proper site selection and management of CO_2 storage projects, the risks to human health and the environment would be minimal. A risk remains, however, that CO_2 could leak from a deep storage formation into overlying shallow potable groundwater aquifers. The buoyant supercritical CO_2 fluid would undergo a phase transition during transit and would reach shallow strata as a gas, where it would partially or completely dissolve into the groundwater. The ambient modal partial pressure of CO_2 in potable water aquifer in the United States is around 10^{-2} bar, which higher than that in atmosphere (Apps et al., in review). After ingress of CO_2, the partial pressure could increase considerably, e.g., up to 5–10 bars in shallow aquifers 50 to 100 m deep. Such increases in $P(CO_2)$ would correspondingly increase the concentration of dissolved carbonate and lower pH over those initially present in the aquifer. This process

by itself would not normally be of concern, but the decrease in pH in the aquifer could adversely affect water quality.

Decreasing pH enhances the solubility of many minerals, including those containing significant concentrations of hazardous trace elements, including lead or arsenic, which occur—in trace amounts—ubiquitously in crustal rocks (Apps et al., in review). The resulting increase in concentration of hazardous trace elements can detrimentally affect groundwater quality, possibly to the extent that drinking water standards are exceeded. Decreasing pH could also mobilize hazardous trace elements adsorbed on clays, iron oxyhydroxides, or the surfaces of other rock-forming minerals.

Limited research conducted so far demonstrates the vulnerability of potable groundwater resources to CO_2 intrusion and that the risks associated with large-scale CO_2 storage in deep geologic formations should be assessed. For example, Kharaka et al. (2008) reported on a field experiment with CO_2 injection into a shallow aquifer in Montana. Preliminary groundwater analyses clearly show that increased acidity due to increases in CO_2 partial pressure leads to the mobilization of many hazardous trace metals as well as iron and manganese. Smyth et al. (2008) observed decreases in pH and increases in cation concentrations in laboratory batch experiments with diverse aquifer rocks exposed to CO_2 charged water. McGrath et al. (2007) evaluated the potential impact of carbon dioxide generated in municipal solid waste (MSW) landfill gas on the release of cadmium from uncontaminated native soils. Based on soil leaching experiments and geochemical modeling, the authors concluded that the observed increases in aqueous cadmium in the

field were likely caused by CO_2 dissolution into the groundwater, resulting in mobilization of cadmium from naturally occurring otavite (or cadmium carbonate) in the soils.

To date, the potential geochemical effects of CO_2 intrusion into shallow potable groundwater have not been investigated systematically. Wang and Jaffe (2004) conducted reactive-transport simulations to assess the impact of CO_2 intrusion into an aquifer containing significant volume fraction of galena (PbS). Their results suggest strongly increased lead concentration levels because of galena dissolution, in poorly buffered aquifer to levels higher than the maximum contaminant level (MCL) for lead defined by the U.S. Environmental Protection Agency (EPA). The authors, however, intended their study only to illustrate the potential adverse effects of CO_2 intrusion on water quality. Their simulations do not necessarily represent realistic conditions as their model geochemical system is greatly simplified. Thus, while Wang and Jaffe (2004) highlight a potential concern, it is not clear to date how severe and widespread the problem would be in reality. In another study, Carrol et al. (2008) conducted reactive transport simulations to evaluate the impact of CO_2 intrusion into the High Plains Aquifer in the United States. However, the purpose of their study was to understand only the resulting pH changes and to evaluate the ability of detecting the resulting acidic plume; the issue of mobilization of hazardous trace elements was not addressed.

The present paper is the third of a series. Apps et al. (2008) and Apps et al. (in review) summarized a thermodynamic evaluation of the behavior of nine hazardous trace

elements of interest to EPA using 38,000 groundwater quality analyses taken from the NWIS database, conducted as a starting point for understanding and predicting the impact of CO_2 intrusion on groundwater quality. This evaluation was part of a study undertaken on behalf of the U.S. Environmental Protection Agency and was reported more fully in the first half of a comprehensive technical report to EPA (Birkholzer et al., 2008). The present paper focuses on the mobilization of As and Pb by CO_2 intrusion, which constitutes the second part of the study reported in Birkholzer et al. (2008)..

In conducting this study, we hoped to accomplish several objectives. First and foremost, we wished to establish whether leakage of CO_2 into potable water aquifers could constitute a serious threat to potable water quality, especially regarding the behavior of two of the most problematic hazardous elements, As and Pb. In meeting this objective, we necessarily had to consider the existing regulatory framework regarding drinking water standards. Secondly, we wished to establish what were the requirements for modeling such a complex geochemical system, and what critical scientific and technical issues limited our meeting the first objective. Specifically, our scientific objective is to better understand, for a range of relevant aquifer conditions, the complex processes affecting this process. We also predict the distribution of these trace elements in time and space and quantify related uncertainties. We attempt to address these issues by simulating reactive transport under a variety of CO_2-release scenarios and aquifer conditions including the initial abundance and distribution of lead and arsenic, aquifer mineralogy and initial water chemistry and oxidation state. These conditions were based on the comprehensive thermodynamic evaluation of more than 38,000 groundwater quality

analyses from potable aquifers throughout the United States (Birkholzer et al., 2008; Apps et al., 2008; Apps et al., in review) using a version of the EQ3/6 code (Wolery, 1993) .

Thirdly, we hoped, through development and refinement of a reactive transport simulator, eventually to be in a position to test our geochemical model against actual field conditions at any specific site, to establish whether the model concepts were valid or required further refinement. As the following evaluation attests, many parameters necessary for development of the model are either poorly known, or not known at all, and therefore estimates had to be made with varying degrees of confidence. Furthermore, the resulting model represents a generalization of all shallow arenaceous potable water aquifers, the constituent parameters describing the system having substantial variability. The described simulations are therefore illustrative rather than being representative of what might happen following CO_2 intrusion into shallow potable water aquifers. We naturally hope that readers will be informed of the possibilities as well as the challenges that such modeling represents.

2. Modeling approach

2.1. Simulator

The multiphase flow and reactive transport modeling is performed with the TOUGHREACT code (Xu et al., 2006). The simulator was developed by introducing

reactive chemistry into the existing framework of a non-isothermal multi-phase multi-component fluid and heat flow code, TOUGH (Pruess et al., 1999). A specific fluid property module for CO_2 sequestration includes a comprehensive description of the thermodynamics and thermophysical properties of a H_2O–NaCl-CO_2 system (Pruess, 2005). Flow processes can be modeled isothermally (as done in this study) or non-isothermally, and phase conditions may include a single (aqueous or CO_2-rich) phase, as well as two-phase mixtures. Depending on the temperature-pressure conditions, CO_2 may be in a supercritical or gaseous form. Aqueous chemical complexation and gas (CO_2) dissolution/exsolution are assumed to be at local equilibrium. For the conditions assumed in this study, the intrusion of gaseous CO_2 into a freshwater aquifer is modeled as a two-phase flow system, with instantaneous dissolution and equilibration of CO_2 into the aqueous phase. The migration of any excess gaseous CO_2 within the aquifer is driven mainly by buoyancy forces.

The geochemical model implemented in TOUGHREACT accounts for a variety of equilibrium and kinetic chemical reactions (Xu et al., 2005; 2006). Aqueous complexation, acid-base, redox, and cation exchange are assumed to be in thermodynamic equilibrium. The CO_2(aq) activity and CO_2(gas) fugacity coefficients are determined as functions of pressure, temperature, and salinity, with details given in Xu et al. (2005). The thermodynamic data incorporated in TOUGHREACT are based on the equilibrium constants for aqueous species and minerals given in the EQ3/6 V7.2b Data0.dat database (Wolery, 1993), but with many substitutions and changes (Xu et al., 2005; 2006), including those incorporated in Data0.dat.YMPv4.0 qualified by the U.S.

Department of Energy for the Yucca Mountain Project and changes incorporated specifically in response to the needs of this study (Birkholzer et al., 2008; Apps et al., 2008; Apps et al., in review). For kinetically controlled mineral dissolution and precipitation, a general form of rate law is used based on that proposed by Steefel and Lasaga (1994). The TOUGHREACT version described in Xu et al. (2005; 2006) was the starting point for the modeling studies performed in this study. However, the code was expanded by including a surface complexation model for the calculation of desorption/adsorption to match the requirements of this study.

2.2. Geochemical model definition

The initial conditions specified for the geochemical model, i.e. the initial abundance and distribution of hazardous trace elements, aquifer mineralogy, initial water chemistry, oxidation state, and the geochemical parameters utilized in the reactive transport simulations are based on a literature and data review of potable water aquifers in the United States (Birkholzer et al., 2008; Apps et al., 2008; Apps et al., in review). The steps taken in developing the geochemical model included (1) a review of the literature in order to identify potential mineral hosts controlling the concentrations of hazardous trace elements in groundwaters, (2) an evaluation of the natural abundances of hazardous trace elements in sedimentary formations hosting potable water, (3) development of an extensive thermodynamic database for relevant minerals, aqueous species and site complexation constants, and (4) a geochemical and thermodynamic evaluation of potable groundwater quality analyses from aquifers throughout the United States.

As in any numerical simulation study, reliable model predictions can only be achieved when model parameters are both realistic and representative, and when all relevant processes are adequately incorporated. While a significant effort was made in this study to develop an appropriate geochemical model for risk evaluation, the applicability of this model is limited by incomplete knowledge and uncertainties associated with the thermodynamic and kinetic parameters controlling the dissolution/precipitation and desorption/adsorption behavior of hazardous trace elements in aquifer host rocks.

2.2.1. Mineral hosts for hazardous trace elements

In order to identify which minerals are most likely to act as the primary thermodynamic controls in determining the concentrations of the hazardous trace elements in groundwaters, more than 38,000 groundwater analyses from the USGS National Groundwater Information System (NWIS) database were evaluated using the EQ3/6 software (Wolery, 1993), details of which are given in Birkholzer et al. (2008), Apps et al. (2008) and Apps et al. (in review). According to this evaluation, it is likely that galena (or occasionally clausthalite, PbSe) controls the aqueous concentration of lead in reducing groundwaters, while cerussite ($PbCO_3$) is the primary thermodynamic control under oxidizing conditions. We also concluded that arsenian pyrite ($FeS_{2-x}As_x$) is probably the dominant host for arsenic under the reducing conditions predominant in most aquifers. Subsequent modeling studies presented below, show, however, that a

significant proportion of the As may be distributed on adsorption sites on clays and ferric oxyhydroxides, the actual distribution depending on the mineralogy of any given aquifer. The mineralogy of the host rock of a potable aquifer can have a significant influence on the water quality, and similarly impact on the nature of compositional changes due to the ingress of CO_2. Modal mineralogies were therefore specified on the basis of sedimentological classifications, and these were augmented with the trace quantities of the minerals identified as being at equilibrium with the selected hazardous trace elements (Birkholzer et al., 2008). An arenite with a mineralogical composition typical of those hosting potable groundwaters along the Eastern Coastal Plain of the United States (see Table 1) was selected for the reactive transport simulations described in this paper.

2.2.2. Thermodynamic data

The thermodynamic data incorporated in the TOUGHREACT version described in Xu et al. (2005; 2006) are not sufficient for adequately modeling the complex chemistry associated with the behavior of hazardous trace elements in groundwater. Therefore, the thermodynamic database was significantly expanded as described in Birkholzer et al. (2008). Table 2 lists the aqueous complexes considered and their dissociation constants. Although most constants were taken from the EQ3/6 V7.2b database (Wolery, 1993) and subsequent modifications, others involving complexation by hazardous metals were compiled from an earlier literature review, as described in Birkholzer et al. (2008), especially those for arsenic oxyanions and arsenic and lead sulfide and selenide oligomeric complexes. Table 3 lists the solubility products of minerals hosts and minerals

containing lead and arsenic, as compiled in Birkholzer et al. (2008). Note that aqueous complex dissociation reactions and mineral dissolution/precipitation reactions are given in terms of the primary species: H_2O, H^+, Ca^{2+}, Mg^{2+}, Na^+, K^+, Fe^{+2}, Pb^{+2}, HS^-, H_3AsO_3(aq), HSe^-, AlO_2^-, Cl^-, SO_4^{2-}, HCO_3^-, HPO_4^{-2}, O_2(aq) and SiO_2(aq).

Specific consideration was given to the thermodynamic data of the metal sulfide minerals and aqueous complexes and the corresponding metal selenide minerals and aqueous complexes. Published values for K_s for galena (PbS) showed that discrepancies between those derived from solubility measurements, when compared with those based on thermochemical measurements, were so large that meaningful predictions of galena solubility in shallow potable groundwaters at ambient temperatures would not be possible unless the conflict were resolved. The conflict was resolved by accounting for the presence of an oligomeric neutral complex PbS(aq) in solution. Assuming the correctness of Log K(galena), based on the consistency of independent sets of thermochemical data, the dissociation constant of PbS(aq) was estimated from linear regression of a correspondence plot between Log $K(MS)_s$ versus Log $K(MS)_{aq}$, where M = Cd, Cu, Fe, Hg, Mn, Ni and Zn. The value calculated for Log $K(PbS)_{aq}$, -5.5, is consistent, within the overall uncertainty of the analysis, with independent measurements by Rozan et al. (2003). With the derived Log $(PbS)_{aq}$ and Log K_s(galena) = -14.87, derived from thermochemical measurements by Robie and Hemingway (1995), the saturation index (SI) with respect to galena was calculated for the potable groundwater analyses selected from the NWIS database. However, a satisfactory correlation was not achieved without also taking into account the existence of a parallel set of oligomeric neutral selenide and

charged selenide complexes in solution for Cd, Fe, Hg, Pb, As, Sb and Zn. Details concerning the estimation of these selenide complexes are given in Birkholzer et al. (2008, Appendix E). After inclusion of selenide complexes in the evaluation of potable groundwater analyses, the modal value of SI(galena) indicated an apparent oversaturation by less than half an order of magnitude, a closing error well within the overall uncertainty of the geochemical model employed in the study.

For simulation purposes, K_s(galena) was calibrated to match the modal SI of galena from the above noted measurements of Pb concentrations in potable groundwaters, and the derived value for Log K_s(galena) = -14.4 accepted as listed in Table 3. The purpose in making this correction is to mitigate the impact of uncertainties in the thermodynamic data on simulated predictions of perturbations in Pb concentration due to CO_2 intrusion as described further in Section 4, below. This approach is justified within the context of this study, because regulatory authorities such as EPA are more interested in changes in hazardous metals concentrations relative to specified MCLs due to CO_2 intrusion in potable groundwaters. In Apps et al. (in review), we illustrate both calibrated and uncalibrated predictions, and show that even the uncalibrated model predictions are consistent with field data derived from 38,000 NWIS groundwater quality analyses and observed mode of occurrence of Pb within the uncertainties of the geochemical model and the natural variability of groundwater chemical compositions.

A common cause of arsenic contamination in aquifers arises from the oxidation of arsenian pyrite (Utsunomiya et al., 2003; Arthur et al., 2005). Reich and Becker (2006)

formulated a theoretical solid-solution model quantifying arsenic substitution for sulfur in both pyrite and marcasite. Time constraints prevented the incorporation of this model in the TOUGHREACT simulator. Instead, we incorporated in the TOUGHREACT database an arsenian pyrite solid solution with a stoichiometry equivalent to 0.025 mole fraction substitution of S by As to give a formula: $FeAs_{005}S_{1.95}$. The thermodynamic properties of this solid solution were then calculated, assuming the presence of an ideal solid solution, using the accepted thermodynamic properties of pyrite, and the revised properties of arsenopyrite (FeAsS) given by Pokrovski et al. (2002). An empirical correction factor was applied to the resulting arsenopyrite solubility product by adjusting the predicted As concentration to the modal arsenic concentration in potable groundwater samples from the NWIS database, in a procedure similar to that for galena outlined above.

Minerals other than arsenian pyrite might act as sources of dissolved As and Pb during acidification of the aquifer by CO_2. For example, As could be released from goethite (FeOOH), if present in solid solution as is quite possible. Unfortunately, while an abundant literature provides all manner of details regarding adsorptive processes on goethite and other ferric oxyhydroxides, critical information regarding the structural incorporation of As in solid solution appears to be unstudied. Therefore, we are in no position to account for remobilization of As due to the dissolution of goethite, other than to account for As adsorption/desorption on goethite, as discussed in the following paragraphs.

In our model aquifer, we included small concentrations of calcite ($CaCO_3$). We make no claims as to the origin of interstitial calcite in arenite, which could have been either authigenic or diagenetic in origin, the process undoubtedly affecting the solid solution concentrations of trace elements including both As and Pb. If we assume a marine origin, then some crude estimates of both As and Pb concentrations might be made. With respect to lead, Pitts and Wallace (1994) established a correlation between the concentration of Pb in seawater and the concentration of Pb in a bivalve shell. Assuming the concentration of Pb in seawater in offshore seawater to be 50 ng/kg (Reimer and Miyazaki, 1992), we obtain a concentration of ≈ 0.5 ppm Pb in shell calcite. The dissolution of calcite caused by the increase in $P(CO_2)$ from 10^{-2} to 10 bar would result in an increase in Pb concentration by ≈ 10^{-10} mol/kg H_2O, which is trivial. We therefore believe that our neglect of heavy metal contributions to the aqueous phase as a result of carbonate dissolution is justified. Similar arguments can be advanced with respect to arsenic. Henke (2009), citing Matschullat (2000), indicated that carbonate sedimentary rocks contain only 1-1.5 mg As/kg, and those that contain higher concentrations are contaminated with sulfides [e.g., arsenian pyrite]. Furthermore, Roman-Ross et al. (2006) showed, that "…in the presence of high As(III) concentrations, an average concentration of 30±6 mM/kg of As(III) could be incorporated into the calcite structure." Under ambient conditions of potable water aquifers, substitution of As(III) in calcite would therefore also be ≈ 1–2 mg As/kg calcite. In our simulations, the contribution of As in groundwater due to calcite dissolution under $P(CO_2)$ = 10 bar would be ≈ 10^{-9} mol/kg H_2O, which is trivial.

In addition to changes in the thermodynamic data for solid phases and aqueous complexes, we also modified the code to account for surface complexation. Adsorption via surface complexation has been widely studied (Dzombak and Morel, 1990; Lutzenkirchen, 2006) and is a key process with respect to the fate and transport of heavy metals (for example, Bradl, 2004) or other hazardous trace elements such as arsenic (Goldberg, 2002; Goldberg et al., 2005; Manning and Goldberg, 1997). We have therefore incorporated into TOUGHREACT a model considering adsorption via surface complexation, using non-electrostatic, constant capacity and double layer models (Dzombak and Morel, 1990). The surface complexation model implemented was verified by comparison with other codes such as PHREEQC (Parkhurst and Appelo, 1999) and CRUNCH (Steefel, 2001). In this study, a non-electrostatic surface complexation model is used.

Adsorption of heavy metal (and arsenic) ions on minerals is influenced by a variety of factors, the most important being pH, type, and speciation of metal ion involved, as well as competition between different ions (Bradl, 2004). In this study, we consider goethite, illite, kaolinite, and smectite as principal adsorbents, mainly because these minerals have strong adsorption capacities with respect to lead and arsenic. A literature analysis was conducted to determine relevant surface complexation reactions and their thermodynamic constants for these cations and minerals. Measured parameters under conditions (ionic strength and pH) analogous to potable groundwater are used in the current study. Table 5 lists the surface complexation reactions of lead on different minerals, while Table 6 lists those for arsenic. Specific surface area and site density are the other two important

parameters affecting adsorption (Table 7). It should be noted that we did not include in our model the adsorption of either As or Pb on calcite, as it is well known that oxyhydroxide and clay minerals tend to be stronger adsorbents.

2.2.3. Kinetic data

Reactive transport modeling requires not only a conceptual understanding of the mechanisms involved in the nucleation, precipitation, and dissolution of the suite of participating minerals, but also quantitative estimates of relevant kinetic parameters. TOUGHREACT (Xu et al., 2006) uses a general form of rate expression (Lasaga et al., 1994; Steefel and Lasaga, 1994):

$$r = kA\left[1-\left(Q/K\right)^{\theta}\right]^{\eta} \quad (1)$$

where r is the kinetic rate (positive values indicate dissolution, and negative values precipitation), k is the rate constant (moles per unit mineral surface area and unit time) which is temperature dependent, A is the specific reactive surface area per kg H_2O, K is the equilibrium constant for the mineral–water reaction written for the destruction of one mole of mineral, and Q is the reaction quotient. The parameters θ and η should be determined by experiments, but are commonly set equal to unity when experimental quantification is unavailable. When θ and η are set to unity, Equation (1) reduces to a form applicable to transition state theory (TST). Equation (1) is a general derivation that is valid for minerals undergoing precipitation or dissolution in the aqueous phase

regardless of composition. While it is true that Steefel and Lasaga (1994) were concerned mainly with processes involving rock-forming minerals, their rate law was presumed to be of general applicability to all minerals, including sulfides. However, research conducted over the past 20 years has shown that this rate law is applicable over the full range of potential degrees of saturation or undersaturation only in a limited set of cases where the reaction rate is controlled by formation of a single activated complex, and where dissolution is indiscriminate, e.g., as from an amorphous solid. The literature is now replete with numerous examples demonstrating that this formulation cannot be used to extrapolate far-from-equilibrium dissolution rates to conditions close to saturation (Lasaga and Luttge, 2003). However, under the conditions of our simulations, deviations from equilibrium result in affinities of the order of $\leq \pm 5$ kcal/mol, which generally falls within the range where incremental growth or dissolution occurs at kink sites on crystal steps or edges. Both theoretical considerations and experimental studies indicate that such mechanisms of crystal growth or dissolution commonly occur through a single rate-controlling step, which can be fitted by an equation of the same form as that which describes by TST. See also Lasaga (1998; p. 186-191, p. 611-617).

Beyond a critical affinity, nucleation of etch pits at defect sites leads to accelerated dissolution due to the propagation of multiple step waves (Lasaga and Luttge, 2001), and the simple TST formulation is no longer applicable. At even higher affinities, indiscriminate nucleation of dissolution sites occurs over the exposed faces of the crystal leading to a maximum dissolution rate independent of affinity. The rate laws governing these dissolution mechanisms are not additive, but substitutive (Luttge, 2006).

Furthermore, in contrast to TST dissolution near equilibrium, the values of the rate constants are not applicable to corresponding precipitation mechanisms. Thus, dissolution under TST rate formulations near equilibrium differs, not only mechanistically, but can, and usually are, orders of magnitude slower than far-from-equilibrium rates. As Lasaga and Luttge (2001) note, "…measurements of rates in the field will yield rates that are orders of magnitude slower than laboratory rates measured far from equilibrium."

The cited dissolution mechanisms are equally applicable to both silicate and sulfide minerals, except that most sulfide minerals are semi-conductors, and therefore corrosion can take place preferentially at anodic sites while affording cathodic protection elsewhere on the crystal face. However, in the limiting case, where affinity approaches zero, the TST formulation should be generally applicable, and we believe that the rate law proposed by Steefel and Lasaga (1994) is appropriate for modeling sulfide dissolution or precipitation, especially in relation to perturbations induced by changes in CO_2 partial pressure. For example, the thermochemical perturbation induced by the instantaneous imposition of $P(CO_2)$ = 10 bar under potable water aquifer conditions leads to undersaturation with respect to pyrite and an induced affinity of only -2.75 kcal/mol, which is within acceptable limits for the TST formulation.

Although not necessarily applicable in all cases, the kinetic rate constants can usually be summed from three mechanisms (Lasaga et al., 1994):

$$k = k_{25}^{nu} \exp\left[\frac{-E_a^{nu}}{R}\left(\frac{1}{T}-\frac{1}{198.15}\right)\right] + k_{25}^{H} \exp\left[\frac{-E_a^{H}}{R}\left(\frac{1}{T}-\frac{1}{198.15}\right)\right]\alpha_H^{n_H} + k_{25}^{OH} \exp\left[\frac{-E_a^{OH}}{R}\left(\frac{1}{T}-\frac{1}{198.15}\right)\right]\alpha_H^{n_{OH}} \quad (2)$$

where subscripts *nu*, *H* and *OH* indicate neutral, acid, and base mechanisms, respectively, E is the activation energy, k_{25} is the rate constant at 25 °C, R is gas constant, T is the absolute temperature, a is the activity of the species, and n is a power term (constant). Such a summation is permissible, provided that the component rate mechanisms do not involve dissolution or precipitation from crystallographically distinct sites on the mineral surface.

Mineral dissolution and precipitation rates are products of the kinetic-rate constant and reactive surface areas as represented by Eq. (1). The parameters used for the kinetic rate expression are given in Table 4. Calcite and anhydrite are assumed to react at equilibrium because their dissolution and precipitation rates are rapid relative to the time frame being modeled. The mineral reactive-surface areas (except those for illite, kaolinite, smectite and goethite) were taken from Xu et al. (2007; 2006), based on the work of Sonnenthal et al. (2005). These values are two orders of magnitude smaller than surface roughness-based estimates because typically only part of mineral surface is involved in the reaction (Xu et al., 2007). The surface areas of illite, kaolinite, smectite and goethite were taken from published BET surface area (Bradbury and Baeyens, 2005; Gu and Evans, 2007; Lackovic et al., 2003; Muller and Sigg, 1991) in conformity with the values used for surface complexation reactions in desorption/adsorption processes. Although the effective reactive surface area for mineral dissolution/precipitation and the surface area responding to adsorption/desorption are not necessarily equivalent, no theoretical or practical basis allows us to make such a distinction and therefore they are treated as

equivalent. Kinetic rate parameters for most rock-forming minerals listed in Table 4 were taken from (Palandri and Kharaka, 2004). which are based mainly on experimental studies conducted under far-from-equilibrium conditions. These kinetic rate parameters are therefore expected to be high in relation to those expected to operate in the field, and the measured dissolution mechanism could differ from that assumed to be represented by Equation (1). However, the impact of such uncertainties on the results of the present study is insignificant.

In the present study, we wish to simulate the anoxic dissolution of arsenian pyrite by aqueous ferric complexes under anticipated conditions along the pyrite/goethite redox buffer between pH = 5.5 and 7.5, where, log $p(O_2)$ (bar) is in the range from -67 – -65, and where total Fe(III) in solution is dominated by the FeOOH(aq) complex with a concentration of about 10^{-12} mol/kg H_2O. An abundant literature describes experimental studies of the irreversible dissolution of pyrite under very acid and highly oxidizing conditions, i.e., in the presence of significant $P(O_2)$ or substantial concentrations of ferric ion, e.g., see Rimstidt and Vaughan (2003) and reviews cited therein. A similar, although more restricted set of studies have been made with respect to the irreversible dissolution of arsenopyrite (Walker et al., 2006; Yu et al., 2007; McKibben et al., 2008) and galena (Acero et al., 2007). However, none of these studies are applicable to our simulations, as there is no justifiable basis for assuming that the observed rate dependencies on dissolution can be extrapolated to near reversible conditions represented by our simulations. Unfortunately, we know of no published studies that approach conditions of reversibility involving the anoxic dissolution of either pyrite or arsenopyrite under redox

conditions approaching that of the pyrite/goethite buffer. We therefore resorted to a study of the literature relating to the rates of oxidation of pyrite and arsenopyrite under conditions closest to those represented in our simulations in order to establish an upper bound to the hypothesized reaction rate constant for the dissolution or precipitation of arsenian pyrite. With respect to pyrite oxidation by air ($P(O_2)$ = 0.21 bar) at pH = 7.6 – 8.6, Nicholson et al. (1990), using sulfate to monitor the rate of dissolution, gave an initial rate constant, free of a diffusion controlling surface layer, $k \approx 1.6\times10^{-9}$ mol/(m^2.s). According to these investigators, the rate dependence is appropriately linear when $P(O_2)$ < 0.05 . The dissolution rate under anoxic conditions would therefore be << 10^{-9} mol/(m^2.s). Moses and Herman (1991) estimated that the initial rate of pyrite oxidation by Fe(III) under anoxic conditions at pH =6 or 7 to be 0.5 –1.5 x 10^{-8} mol/(m^2.s), but that adsorption of Fe(II) subsequently inhibited further dissolution. With respect to arsenopyrite oxidation, only the studies by Walker et al. (2006) and Yu et al. (2007) have any relevance to our modeling. The former conducted dissolution experiments using unbuffered influent solutions with narrow spread in pH (5.7 - 7.7) using As as the primary monitor of reaction rate. They determined a $P(O_2)$-independent steady-state rate after 15 hr to be 6.8 x 10^{-11} mol/(m^2.s). This reaction rate is somewhat lower than those cited for pyrite under comparable conditions. Yu et al. (2007) conducted a more comprehensive evaluation of arsenopyrite using As release as a measure of oxidation rate. They established a $P(O_2)$-dependent, pH independent steady-state rate, $r = 10^{-7.4}(mO_2)^{0.45}$ mol/(m^2.s) at 25 C. At log mO_2 = -5, the minimum O_2 concentration used, this translates into a rate = 2 x 10^{-10} mol/(m^2.s) At lower mO_2, it is likely that the oxidation rate becomes independent of $p(O_2)$, but this transition does not appear to have

been investigated, except perhaps by Walker et al (2006), but where iron hydroxide precipitation might have interfered with measured dissolution rates. Given the magnitudes of the uncertainties associated with such experiments, the difference in dissolution rates between the pyrite and arsenopyrite cannot be considered significant. McKibben et al. (2008) conducted experiments that differ markedly from those represented in our modeling, i.e., at low pH (2.0 – 4.5), high ferric ion concentrations (1.8 x 10^{-4} - 1.8 x 10^{-3} mol/) and high $P(O_2)$ (log $P(O_2)$ = -1 and 0). Because conditions were so acid, neither As nor S could be reliably monitored due to the presumed secondary precipitation of native sulfur or possibly an As-S solid solution. Therefore both the stoichiometry of the reaction and the reaction products differ from those observed by Walker et al. (2006) and Yu et al. (2007). However, the dissolution rate of As reported by McKibben et al. (2008) is independent of pH and given as ≈ 3 x 10^{-9} mol/(m^2.s). This value is generally consistent within experimental error with the reported dissolution rate of arsenic from arsenopyrite given by Walker et al. and Yu et al. (2007), the former tentatively concluding that the dissolution of arsenopyrite under circum-neutral pH conditions is controlled by the slow reduction of water at anodic sites on the arsenopyrite surface. The dissolution rates of both pyrite and arsenopyrite under circum-neutral pH conditions therefore appear to be comparable, and one might therefore assume that arsenian pyrite dissolution rates are insensitive to the presence of As in solid solution.

Having shown that experimental data for the anoxic dissolution of pyrite and arsenopyrite at circum-neutral pH suggests an initial rate < 10^{-9} -10^{-10} mol/(m^2.s) under far-from-equilibrium conditions, we consider its applicability to our modeling. Because these rate

constants were established under conditions far from equilibrium, we can assume that they represent maximum values, and that they are likely to significantly overestimate the near-equilibrium rate constants, but no precedent exists for establishing this rate from current knowledge. It should be noted in passing that Blanchard et al. (2007) conclude that sulfur vacancies should form preferentially next to a substituted As atom in the pyrite structure, which would energetically favor dissolution under oxidizing conditions. Thus, arsenian pyrite might be expected to dissolve more rapidly than pure pyrite in the presence of Fe(III). In contrast, Wolther et al. (2005) conclude that the As(III) in solution not only inhibits the nucleation of pyrite, but that As(III) species adsorb on the pyrite surface and retard its growth. It is clear that further study is required to both resolve and quantify our understanding of the kinetics of arsenian pyrite dissolution or precipitation under near equilibrium conditions. In our modeling, we therefore assume pH independent rate constant of 10^{-12} mol/(m^2.s) between pH 7.5 – 5.5,, which is probably too conservative, but suffices until suitable experiments are conducted to evaluate this rate.

The dissolution/precipitation reaction of arsenian pyrite is represented in our model by the following translation equation:

$$FeAs_{0.05}S_{1.95} + 1.025\ H_2O + 0.0375\ O_2(aq) = 1.0000\ Fe^{+2} + 0.1875\ H^+ + 0.2375\ SO_4^{-2} + 1.7125\ HS^- + 0.0500\ H_3AsO_3(aq) \quad (3)$$

The stoichiometry of the arsenian pyrite is based conservatively on the assumption that the initial concentration of As assumed to be present in crustal rocks is concentrated wholly in 1 wt.% pyrite in the aquifer host rock. The actual reaction stoichiometry

established during reaction progress in our simulator is determined by mass action and mass balance constraints. The participation of O_2(aq) is fictive, and is offset by a coupled reaction involving the reduction of Fe(III) to Fe(II). A TOUGHREACT simulation to determine the actual processes involved in the re-establishment of thermodynamic equilibrium of arsenian pyrite coexisting with goethite upon imposition of $p(CO_2)$ = 10 bars shows that the dominant process involves the dissolution of goethite and reduction of $HFeO_2$(aq) at a concentration of approximately 10^{-12} molal with concomitant oxidation of S_2^{-2}(s) to SO_4^{-2}(aq) and As(-I)(s) primarily to H_3AsO_3(aq) with associated precipitation of secondary siderite and barite. Thus, it is clear that arsenian pyrite dissolution involves the oxidation of pyrite by Fe(III).

The dissolution of galena under the anoxic conditions represented by our model appears to be represented by the reaction:

$$PbS + 2H^+ = H_2S(aq) + Pb^{++} \quad (4)$$

in conformity with the results obtained by Hsieh and Huang (1989) involving the dissolution of PbS in 5 x 10^{-2} *M* $NaClO_4$ solution over a pH range between 2.5 and 9.0 under dark, oxygen-free conditions. The findings of the latter authors were not utilized in our study, as the PbS feed was not characterized crystallographically. Another experimental study by Zhang et al. (2004) was conducted under similar anoxic conditions, but using a supporting electrolyte of 1molar NaCl solution within a pH range between 0.45 and 2, and at fixed temperatures of 25, 50, and 75ºC. Unfortunately, their kinetic results are likely to be influenced by Pb complexation with Cl^-, and the pH range of their study lies well outside that considered in our model. A more recent study by

Acero et al. (2007) involved the dissolution of galena in the presence of air under acid conditions. However, the findings are inapplicable to our study, as their experimental conditions involved irreversible oxidation of galena by O_2 under acid conditions. Nevertheless, the question remains as to whether the presence of dissolved Fe(III) in our study might lead to oxidative dissolution of galena with either partial or total conversion of S(-II) to S(VI). In our model, although we assume a TST rate law with respect to the near-equilibrium dissolution of galena according to reaction (1), we do not discount the concurrent instantaneous oxidation of $H_2S(aq)$ to SO_4^{-2} in the aqueous phase as determined by mass action and mass balance constraints. In our final analysis, rates of dissolution or precipitation of galena are taken from Zhang et al. (2004) which we think are tentative at best , given the lack of experimental data, and this is reflected in our subsequent uncertainty analyses.

3. Model setup

The base model setup for most of the simulations presented here is depicted in Figure 1. The hydrogeological configuration considered is relatively simple. We assume a confined aquifer with a uniform vertical thickness of 10 m at a reference depth of 50 m. The simulation domain comprises an area of 500 m in length and 200 m in width. Water flows from left to right with a pore velocity of 10 m per year. Hydrogeologic properties, as given in Table 8, are homogeneous and constant in time. CO_2 is assumed to migrate from a deeper geological storage site into the aquifer, representing, for example, a local leakage through a fault zone. We assume in the base model a continuous CO_2 leakage

rate of 7.5×10^{-5} kg/s, which corresponds to 2.36 tonnes per year, entering from below over an area of 100 m^2 (10 m × 10 m) at x = 105 m and y = 0 m.

The potential rate of CO_2 leakage into an aquifer may vary over a large range in fields. We have selected the above leakage rate roughly based on the amount of CO_2 that can dissolve into the groundwater without forming a large two-phase zone of gaseous CO_2 and water. Excess CO_2 (i.e., gaseous CO_2 not dissolving into water) would migrate upwards and, in an unconfined aquifer, would escape into the vadose zone without further impacting groundwater quality. In a confined aquifer, which is the situation assumed in this study, excess CO_2 would accumulate and spread out under the confining layer, where it would continue to dissolve into the migrating groundwater.

In the model, the background CO_2 partial pressure was set to 0.005 bar. The concentration of dissolved CO_2 in equilibrium with this partial pressure falls into the range of values calculated from the database analysis described in Birkholzer et al. (2008). The model also assumes reducing conditions with a redox potential of approximately -0.23 V at pH around 7.6, defined by the coexistence of pyrite and goethite. The thermodynamic analysis of potable groundwater reported in Birkholzer et al. (2008) indicates that the majority of samples from the NWIS database represent waters from reducing environments.

4. Results

4.1. Initial geochemical conditions for base model

Each simulation was performed using a two-step procedure. First, an initial equilibration run was conducted with a specified mineralogical composition to establish a quasi-steady-state chemical composition of the groundwater in association with host-rock prior to the intrusion of CO_2. This step also established the distribution of trace elements and other species on the adsorption sites of the specified adsorbent minerals. The simulated duration of the initial equilibration step was 10,000 years, a time period sufficient to bring the specified detrital and secondary rock forming minerals close to equilibrium with respect to the aqueous phase. Complete equilibration of all rock-forming minerals is, however, not achievable, as is also typical in nature, where slow diagenetic alteration proceeds indefinitely at near earth surface temperatures. The aqueous phase composition corresponded closely with the modal composition of some 35,000 potable groundwater analyses taken from the NWIS database (Birkholzer et al., 2008), with the exception of Al and Mg. The underlying cause of this discrepancy is being investigated, e.g., see Zhu et al. (2004a,b) and Zhu and Lu (in press), and relates to the formation of metastable secondary hydroxy aluminum and magnesium silicate alteration products of detrital minerals. The impact of this discrepancy in relation to the behavior of As and Pb in our simulations is negligible

After completion of the initialization step, reactive transport simulations were conducted for the hydrogeological environment shown in Figure 1, with the initial aqueous chemical

composition obtained from the initial equilibrium run. CO_2 intrusion starts at time zero and continues for the entire simulation period of 100 years.

Table 9 shows the initial total aqueous concentration of major constituents and hazardous trace elements obtained from the initial equilibrium run. The calculated total aqueous lead concentration is 1.3×10^{-9} mol/L, which corresponds closely to the modal value of analytical lead concentration in potable groundwaters from the NWIS database (Birkholzer et al., 2008; Apps et al., 2008). The calculated total aqueous arsenic concentration is 4.5×10^{-8} mol/L, which also falls close to the modal value of analytical As concentration observed in potable groundwater analyses from the NWIS database (Birkholzer et al., 2008; Apps et al., 2008).

4.2. Base model results

The CO_2 intruding into the aquifer dissolves instantaneously into the groundwater, although a gas phase evolves after around 3 years close to the area of intrusion, and a small two-phase zone remains during the remainder of the simulation period. The plume of dissolved CO_2, given in Figure 2 as total inorganic carbon (TIC), migrates primarily along the groundwater flow direction, while lateral spreading of dissolved CO_2 is minor. The evolution of pH closely follows the evolution of TIC, with pH decreasing as the concentration of TIC rises. The lowest pH is around 5.6 within the two-phase zone and about 5.9 outside the two-phase zone (Figure 3), which is higher than the expected pH in a system without any buffering capacity. For a non-buffered system, a minimum pH

around 4.5 could be expected. The moderation in pH decrease is caused primarily by the dissolution of calcite.

Our results for the base model suggest that desorption/adsorption of Pb^{+2} ion from mineral surfaces is more important to the increase of aqueous lead concentration than the dissolution/precipitation of galena. Figures 4 and 5 exemplify the complexity of these processes by illustrating the change in the surface complex concentrations for illite. The surface complex concentration is expressed in mol/L solution. Desorption and adsorption constitutes, respectively, the net effects of decreasing and increasing the concentration for all relevant surface complexes. Illite is the most important adsorbent of lead. $Ill^{s}\_OPb^{+}$ is a surface complex of lead on illite that represents the mass of lead on the strong site at the surface of illite, whereas $Ill^{w}\_OPb^{+}$ represents the mass of lead on the weak site at the surface of illite. The increase of $Ill^{s}\_OPb^{+}$ (Figure 4a) compared to initial levels indicates that aqueous lead is adsorbed on the strong site, whereas the decrease of $Ill^{w}\_OPb^{+}$ (Figure 4b) indicates that aqueous lead is released from the weak site on illite. Another important surface complex that adsorbs lead is $Sme^{s}\_OPb^{+}$, which represents the mass of lead on the strong site at the smectite surface.

Figure 5 shows the relative change of total Pb concentration on adsorption sites (which is a summation of the concentration of all lead surface complexes), calculated as:

$$(S^{t} - S^{ini}) / S^{ini} \tag{5}$$

where S^t is the total lead concentration on adsorption sites at a given time *t*, and S^{ini} is the initial total lead concentration on adsorption sites (both given in mol/L solution). Figure 5 indicates that significant desorption of lead occurs in the two-phase zone (depleting the initially sorbed lead by about 60% after 100 years), thereby increasing the aqueous Pb concentration. Less effective desorption occurs further downstream, even though the pH is similarly low. The overall effect of desorption downstream is smaller because the aqueous lead mobilized in the two-phase zone migrates downstream, inhibiting further desorption.

The current model assumes that sorption via surface complexation is in equilibrium whereas mineral dissolution/precipitation is kinetically controlled, as is known that the time for an adsorption reactions to equilibrate is substantially shorter than that for mineral dissolution, in particular when low-solubility minerals such as sulfides are concerned (Selim and Amacher, 1996). The ingress of CO_2 immediately disturbs both sorption and solubility equilibria, but whereas sorption reactions in our simulations re-equilibrate instantaneously, the dissolution/precipitation of a hazardous mineral host is kinetically controlled and much slower. The relatively sudden release of lead from sorption sites therefore increases the aqueous lead concentration so significantly that the solution becomes transiently supersaturated with respect to galena and galena precipitation occurs in the two-phase zone (even though the groundwater becomes more acidic, which could otherwise suggest undersaturation with respect to galena). This is visualized in Figure 6, where the volume fraction change of galena was calculated as:

$$(V^t - V^{ini}) / V^{ini} \quad (6)$$

Here, V^t is the volume fraction of the considered mineral at given time *t*, and V^{ini} is the initial volume fraction. Negative values indicate dissolution, positive values indicate precipitation.

The complex interaction between desorption/adsorption, dissolution/precipitation of relevant minerals, and the dissociation/association of aqueous complexes control the changes in aqueous lead concentration in response to CO_2 intrusion. Figure 7 shows the total aqueous lead concentration profile along the x-axis at y = 0 m for different times. The concentrations of aqueous lead peaks at 3.4×10^{-8} mol/L in the small two-phase zone at the injection location after 5 years, but then decreases to 1.8×10^{-8} mol/L after 50 years. With time, the peak moves incrementally downstream, and falls progressively to 1.6×10^{-8} mol/L after 100 years and eventually approaches a stable value around 1.1×10^{-8} mol/L (2.3 ppb). This value is significantly higher (about one order of magnitude) than the initial concentration, but remains below the MCL, which is 7.24×10^{-8} mol/L (15 ppb).

The relative change of the total arsenic surface-complex concentration shown in Figure 8 indicates that desorption of arsenic occurs in the two-phase zone, increasing its aqueous concentration, whereas adsorption occurs further downstream, thus limiting further concentration increases. Figure 9 shows the volume fraction change of arsenopyrite in solid solution. In contrast to the lead, where the metal-hosting mineral (galena) actually

precipitates out after intrusion of CO_2, arsenic is mobilized by arsenopyrite dissolution in the two-phase zone and, to a lesser degree, in the downstream region. Therefore, in the case of arsenic, the decrease in pH in the two-phase zone causes both desorption of arsenic from the mineral surface (Figure 8) and dissolution of the arsenopyrite component (Figure 9), generating a considerable concentration increase (Figure 10). Further increases of arsenic concentrations downstream of the two-phase zone are limited, because the water arriving from upstream already has an elevated arsenic concentration, the dissolution of the arsenopyrite component becomes less effective, and some aqueous arsenic sorbs back to the mineral surfaces (Figure 8). The maximum concentration almost reaches the MCL (1.33×10^{-7} mol/L or 10 ppb) within the small two-phase zone, and is slightly lower than the MCL within the elongated area of increased acidity downstream of the intrusion location. Notice that mobilization of arsenic, from minerals and from sorption sites, causes only small changes to the initial contaminant mass in the solid phase, even after a time period of 100 years of CO_2 intrusion. Very small amounts of arsenic contained in the aquifer solid phase can provide a long-lasting source of contamination.

The base model results highlight the contrasting distributions of lead and arsenic among the constituent phases within the modeled aquifer, as shown in Table 10. For whereas the calculated initial distribution of Pb in the aquifer shows that it is predominantly contained in the host mineral, galena, with only a very small proportion distributed on adsorption sites, As, in contrast, is distributed primarily on adsorption sites, with arsenian pyrite hosting less than 40%. Our simulation results indicate, however, that the ratio of Pb and

As present as sulfides vs. adsorbing phases does not determine their relative contribution to the Pb and As mobilized by CO_2 intrusion. In a 100-years simulation, neither Pb or As present as sulfides, nor those in adsorbing phase are depleted, their contributions being determined by the respective reaction rates, with adsorption/desorption being rapid and thus controlling the final aqueous concentration of As and Pb after CO_2 intrusion. The model results also show the significant role that clay minerals can play as adsorbents of As and Pb in relation to the ferric oxy-hydroxide, goethite. Therefore, it cannot be presumed that ferric oxyhydroxides are necessarily the predominant adsorption hosts for these two hazardous trace elements. The adsorptive behavior of trace elements must therefore be fully defined for any given aquifer host rock, particularly with respect to minerals with large reactive specific surface areas. It must also be emphasized that the base model results presented here are illustrative rather than being representative, and that future model refinements and confirmatory field studies may modify the distributions shown in Table 10. It is noteworthy that the competition of other species for the sorption sites is ignored in current model. An unreported simulation which includes adsorbed Ca^{+2} and Mg^{+2} indicates that sites occupied by Pb^{+2} only change marginally and the mobilization of Pb^{+2} from sorption due to the drop of pH remains the same. Still a model which includes the adsorption of all possible species is highly desirable in the future.

4.3. Sensitivity analyses

We conducted various sensitivity test to better understand the complexity and to encompass the uncertainty associated with the relevant geochemical processes, including

simulations with/without sorption and varying model parameters such as mineral solubility products, dissociation constants of aqueous complex PbS(aq), surface complexation constants, and kinetic rates. In addition, we varied certain hydrogeological conditions, such as the depth of the freshwater resource, the groundwater flow rate, and the CO_2 intrusion rate. Some of these sensitivity analyses are elaborated below.

4.3.1. Sensitivity to mineral solubility

With galena and arsenian pyrite being the focus in the current model, the solubility products of these trace-element-bearing minerals are the most critical parameters for dissolution-related increases in aqueous concentrations of lead or arsenic. The initial choice for the solubility product of galena, logK = -14.4) was selected based on the thermodynamic evaluation of groundwaters from the NWIS database (see Section 2.2.2). However, the thermochemical data used in the calibration of logK (galena) have uncertainties of ± 1 kcal/mol, which translates into an uncertainty in logK of about 0.7 at 25 ^{o}C. The MINTEQ (Allison et al., 1991) database cites a logK value of -13.97 for galena, which was also the value used by Wang and Jaffe (2004). We therefore conducted a sensitivity run in which a logK value of -13.97 for galena is used.

As mentioned in Section 3, our simulations include two steps: (1) an initial equilibration run, establishing the initial steady-state equilibrium conditions before CO_2 intrusion, and (2) a reactive transport simulation for the chemical evolution after CO_2 intrusion. Increasing the solubility of galena changes the initial distribution of lead in the aqueous

phase and changes the amount of lead adsorbed on mineral surfaces. Table 11 shows that the initial total aqueous lead concentration in the sensitivity run is higher (by a factor of 2.5) than that in the base model. Consequently, the initial total concentration of lead on adsorption sites is also higher, as a result, more desorption occurs upon intrusion of CO_2 (see Figure 11a). The resulting total aqueous lead concentration is significantly higher than that in the base-run (see Figure 11b), but still does not exceed the MCL.

We conducted a sensitivity run in which the base model solubility of arsenian pyrite was decreased by a one-half order of magnitude lower (Figure 12). Decreasing the solubility of the arsenopyrite component has two effects. First, the initial total aqueous arsenic concentration is lower, which also causes the total arsenic concentration on sorption sites to be smaller. Second, the total aqueous arsenic concentration after intrusion of CO_2 is smaller than in the base model, because both desorption from mineral surfaces and dissolution of arsenopyrite are less significant (see Figure 12). A sensitivity run with solubility of arsenian pyrite one-half order of magnitude higher was also conducted. As shown in Figure 12, the initial total aqueous As concentration is already higher than the MCL and subsequently the concentration after intrusion of CO_2 is much higher than MCL.

4.3.2. Sensitivity to sorption

Previous work on the lead mobilization by galena dissolution by Wang and Jaffe (2004) did not consider desorption/adsorption. To explore the sensitivity of system to sorption process, we performed a simulation without sorption process as well as examining the

consequence of lower sorption site density and the sensitivity to variation in surface complexation constant. These effect are discussed in the following sections.

4.3.2.1. Simulations without sorption of lead and arsenic

In the base-run, desorption in the two-phase zone releases lead into aqueous phase, the groundwater becomes supersaturated with respect to galena, consequently galena precipitates. Without sorption, the increased acidity due to the ingress of CO_2 causes dissolution of galena. The lead dissolved close to the injection zone migrates downstream, where galena continues to dissolve due to the lowered pH. As a result, the initially relatively small aqueous lead concentrations in the two-phase continue to build up along the flow path (Figure 13a). The observed trend is, however, very moderate, and lead concentrations are not expected to rise much higher further downstream. This finding is consistent with Apps et al. (2008) and Apps et al. (in review), who conducted equilibrium calculations to determine the increase of galena solubility with the increase of partial pressure of CO_2. Their results suggested that the MCL of lead is unlikely to be exceeded in reducing groundwaters in the case where only galena dissolution were to occur. During the 100 year period shown here, the resulting lead concentration is smaller in the sensitivity run compared to the base-case (Figure 13a), indicating that desorption has the potential to release more lead than dissolution of galena.

The omission of sorption processes has a similarly significant effect on arsenic. Without sorption, the arsenic concentrations increase significantly along the flow path (Figure

13b). The trend seen in the profiles suggests that the MCL for arsenic would be exceeded further downstream. This is in contrast to the base model, where adsorption stabilizes the aqueous arsenic to a relatively uniform level that is smaller than the MCL (Figure 10). Results in the base model show much higher concentrations in the two-phase zone near the CO_2 intrusion location, which is caused by the significant mobilization of initially adsorbed arsenic.

4.3.2.2. Sensitivity run with lower site density

Illite is the most important mineral that adsorbs or desorbs both lead and arsenic in the base-run, we therefore conducted sensitivity analyses to evaluate the impact of varying the site density on illite surfaces (see Figures 14a and 14b), from the initial value of 2.3×10^{-6} mol/m^2 taken from Gu and Evans (2007) to a smaller value of 6×10^{-7} mol/m^2 based on the work of Lackovic et al. (2003). The decrease in site density leads to less effective desorption and thus lower lead and arsenic concentrations (Figures 14a and 14b). Note that in contrast to the base model galena starts dissolving as desorption does not release sufficient lead to cause supersaturation.

4.3.3. Sensitivity to kinetic rate parameters

4.3.3.1. Sensitivity to kinetic rate parameter for galena

In the current model, the dissolution of galena is caused mainly by the increase of acidity as CO_2 intrudes into the aquifer. A literature search for rates of galena dissolution under

anoxic conditions was conducted (Section 2.2.3) and eventually the galena dissolution rate of Zhang et al. (2004) was used in our model. Published values for the galena dissolution rate under anoxic conditions, as determined by laboratory experiments, show a strong pH dependence and vary over several orders of magnitude, e.g., Hsieh and Huang (1989) and Zhang et al. (2004). However, the rate laws for galena dissolution in these two papers differ, i.e., $[H^+]^2$ vs. $[H^+]$ dependence, respectively. Also, no corroborating field estimates are available to substantiate laboratory measurements of reaction rates. Potential discrepancies may result from a lack of understanding of the reaction mechanism, experimental errors, differences in solution chemistry, inaccuracies in reactive surface area and estimates of water-mineral contact area, temperature variability, or biological activity (Brantley and Velbel, 1993). Note that kinetic rate (r) is a product of kinetic-rate constant (k) and reactive surface area (A) (see Eq. 1). The magnitude of the reactive surface area is also highly uncertain, which further aggravates the uncertainty associated with the kinetic rate.

Sensitivity simulations by varying the kinetic rate constant (k) by two orders of magnitude were performed to partially address the issue of large uncertainties in dissolution rates under anoxic conditions. Note that with respect to the rate law used in the current simulations, both the precipitation rate and the dissolution rate is assumed to be of the same magnitude, but of opposite sign, for a given degree of disequilibrium. As discussed in Section 4.2, galena precipitates rather than dissolves upon intrusion of CO_2. It follows that in the sensitivity run, a smaller kinetic rate leads to less precipitation of galena. Consequently, more aqueous lead remains in the aqueous phase after its release

from adsorption sites and the concentration of lead in the two-phase zone is slightly higher than in the base model (Figure 15). The opposite effect is seen with a larger rate constant.

Overall, the simulated concentrations of aqueous lead after 100 years of CO_2 intrusion are rather insensitive to the variation of the kinetic rate, because desorption is the dominant process that controls the evolution of aqueous lead concentration, effectively dampening the effect of mineral precipitation. In order to illustrate how the kinetic rate would affect the aqueous Pb concentration with less dominant sorption, we also performed two sensitivity simulations varying the kinetic rate constant in the absence of sorption (not shown in this paper). Without sorption, an increase in the kinetic-rate constant by two orders of magnitude leads to more effective dissolution, which results in a slight increase of aqueous Pb concentrations after 100 years of CO_2 intrusion.

4.3.3.2. Sensitivity to kinetic rate parameter for arsenian pyrite

As discussed in Section 2.2.3, we estimated that the kinetic rate parameter for arsenian pyrite is $=2.6\times10^{-12}$ mol/(m^2·s), given that the rate of release of arsenic from non-oxidative pyrite dissolution is unavailable, and the available information does not permit further refinement for the purpose of this study. Considering the substantial uncertainty in the kinetic rate of arsenian pyrite, we conducted a sensitivity analysis varying the kinetic-rate constant for arsenopyrite by four orders of magnitude.

Figure 16 shows the sensitivity of aqueous arsenic concentration to the kinetic rate constant of arsenian pyrite. As discussed in the Section 4.2, while desorption of arsenic from sorption sites and dissolution of the arsenopyrite component both release arsenic into the aqueous phase, the contribution due to dissolution is marginal in the base-run. Because a decrease of the kinetic-rate constant makes the contribution of dissolution even more trivial, the total release of arsenic is not expected by the decrease of kinetic rate constant. Sensitivity analyses are conducted only for the case where kinetic rate constant increases. An increase of the rate constant by two order of magnitude does not shown any clear effect on the total release of arsenic while an increase of the rate constant by four order of magnitude results in increased mobilization of arsenic, which shows in a slightly higher aqueous arsenic concentration. Overall, the results are rather insensitive to the kinetic rate constant. As with lead, the dominant process affecting aqueous concentration is desorption/adsorption rather than dissolution/precipitation. For the purpose of comparison, sensitivity simulations were conducted for a case without sorption (not shown in this paper). A two-orders-of-magnitude higher kinetic rate leads to a strong increase in aqueous arsenic concentration.

4.3.4. Sensitivity to CO_2 leakage rate

The base model assumes a gaseous CO_2 intrusion rate of 7.5×10^{-5} kg/s, which corresponds to 2.36 tonnes of CO_2 per year. To understand the implications of more CO_2 leaking into the aquifer, we performed a sensitivity run with a CO_2 intrusion rate of 6 $\times10^{-4}$ kg/s. With the increased CO_2 intrusion rate, we observe a much larger two-phase

region and a correspondingly larger region with elevated TIC. As a result, CO_2 partial pressure in the two-phase zone is larger than in the base-run and the pH is lower (see Figure 17). This pH decrease has implications for mobilization of hazardous trace elements, giving rise to significant increases in aqueous lead concentrations (Figure 18a), and moderate increases in arsenic concentrations downstream (Figure 18b). Note that these simulations are two-dimensional depth-averaged model. Thus, the vertical variation in gaseous and aqueous CO_2, as well as the vertical variation in the resulting geochemical changes, has been neglected so far. This raises questions regarding the limitations of the 2D assumption. An increased CO_2 leakage rate (by a factor of 8) has shown that a large CO_2 gas plume is generated, as evident in the 2D results, suggesting that buoyancy forces are relevant and that a 3D model should provide a better simulation. Birkholzer et al. (2008) and Apps et al. (in review) conducted 3D simulations, which indicate that the buoyancy of CO2 leads to accumulation of a gaseous plume at the top of the aquifer, and induces significant vertical variation in gas saturation. The resulting impact on aqueous contamination is influenced by the general pattern of the CO_2 plume (e.g., the spreading of the plume at the top of the aquifer) and the subsequent migration of CO_2-charged and contaminated water further downstream. Maximum concentrations are moderately higher than that obtained by 2D model, mostly at the top of the aquifer.

5. Summary and conclusion

As an effort to evaluate the potential risks associated with geologic sequestration of CO_2, reactive transport simulations were conducted to evaluate to what extent lead and arsenic

might be mobilized in shallow potable-water aquifer and the mechanisms behind it. Various sensitivity studies were conducted under various geochemical and hydrological conditions. The impact of CO_2 intrusion was modeled for a synthetic hydrogeological situation in a representative shallow confined potable aquifer while considering continuous ingress of CO_2 for a time period of 100 years. The following conclusions are made from our simulations:

1. CO_2 ingress into a shallow aquifer can lead to significant mobilization of lead and arsenic, contaminating the groundwater near the intrusion location and further downstream. While substantial increases in aqueous concentrations are predicted to occur compared to the initial water composition, the maximum contaminant level for arsenic in groundwater is exceeded in only a few cases, whereas the maximum contaminant level for lead is never exceeded at all.

2. Desorption/adsorption via surface complexation is arguably the most important process controlling the fate of hazardous trace elements mobilized by CO_2 leakage. In a case without sorption processes, the resulting long-term contamination of the aquifer is less significant near the region where CO_2 enters, while aqueous concentrations increase continuously along the flow path as acidic water migrates further and more dissolution occurs. The relative effects of dissolution/precipitation versus desorption/adsorption is determined by many factors, including adsorption parameters, reaction kinetics, aqueous complexation processes, and mineral solubility constants.

3. Moderate to strong sensitivities in the resulting lead and arsenic concentrations are associated with some geochemical parameters such as the solubilities of hazardous-constituent-bearing minerals, the kinetic rates for precipitation and dissolution, and the aqueous complexation constants. The initial volume fraction of trace- element minerals that contain lead and arsenic as essential components is less relevant. As long as these trace minerals have not been completely dissolved (a very slow process), the contamination of an aquifer via dissolution and/or desorption is fairly independent of the initial mineral volume.

4. An increase in the leakage rate leads to increases in partial pressure of CO_2 and consequently lower pH and higher maximum contaminant concentrations in the aquifer. The resulting impact on aqueous contamination is influenced by the general pattern of the CO_2 plume and the subsequent migration of CO_2-charged and contaminated water further downstream.

It is noteworthy that simulations have conducted for several alternative host rock mineralogies (Birkholzer et al., 2008). Model results indicate that (1) the amounts of illite and smectite contained in different mineralogies have major effects on the final aqueous concentration of lead and arsenic because illite and smectite are the most important adsorbent, (2) The complete absence or deplete of any carbonate decreases the pH buffering capacity and lowers pH incrementally compared with the bases case, consequently the final aqueous concentration of lead and arsenic could be higher.

We made an attempt to better understand the complex conditions and processes affecting vulnerability of representative and relevant aquifer types in the case of CO_2 intrusion. A comprehensive set of sensitivity simulations was performed for different hydrological, geochemical, and mineralogical conditions (Birkholzer et al., 2008), only a small subset of which is presented here. Note that even the most comprehensive sensitivity study can neither encompass all possible conditions and scenarios, nor can it account for the considerable uncertainty inherent in geochemical parameters. For quantitative predictions to be useful in a risk assessment, our simulation study should be followed up with site-specific model predictions, supported by integrated laboratory and/or field experiments that can test uncertain model assumptions and parameters.

Acknowledgements

We thank the US Environmental Protection Agency, Office of Water and Office of Air and Radiation, for funding this study under an Interagency Agreement with the U.S. Department of Energy at the Lawrence Berkeley National Laboratory, Contract No. DE-AC02-05CH11231.

References

Acero, P., J. Cama and C. Ayora, 2007. Rate law for galena dissolution in acidic environment. Chemical Geology, 245, 219-229.

Allison, J.D., D.S. Brown and K.J. Novo-Gradac, 1991. MINTEQA2/PRODEFA2, A geochemical assessment model for environmental systems: Version 3.0 user's

manual, Environmental Research Laboratory Office of Research and Development, U.S. Environmental Protection Agency.

Apps J.A., L. Zheng, Y. Zhang, T. Xu, J.T. Birkholzer. 2009. Evaluation of Groundwater Quality Changes in Response to CO2 Leakage from Deep Geological Storage. Transport in Porous Media, in review.

Apps J.A., Y. Zhang, L. Zheng, T. Xu, J.T. Birkholzer. 2008. Identification of Thermodynamic Controls defining the Concentration of Hazardous Elements in Potable Ground Waters and the Potential Impact of Increasing Carbon Dioxide Partial Pressure. 9th International Conference on Greenhouse Gas Control Technologies, November 2008, Washington, D.C., Physics Procedia.

Arthur, J.D., A. A. Dabous, and J. B. Cowart (2005), Water-rock geochemical considerations for aquifer storage and recovery: Florida case studies. In: Underground Science and Technology, C.-F. Tsang and J. A. Apps, eds., Development in Water Sciences, 52, Chapter 24., pp. 327–339, Elsevier, Amsterdam.

Bachu, S., 2000. Sequestration of CO2 in geological media: criteria and approach for site selection in response to climate change. Energy Conversion and Management, 42, 953–970.

Birkholzer, J.T., J.A. Apps, L. Zheng, Y. Zhang, T. Xu and C.-F. Tsang., 2008. Research Project on CO2 Geological Storage and Groundwater Resources: Water Quality Effects Caused by CO2 Intrusion into Shallow Groundwater. Technical Report LBNL-1251E, Lawrence Berkeley National Laboratory, Berkeley, CA.

Blanchard, M., Alfredsson, M., Brodholt, J., Wright, K. and Catlow, C.R.A., 2007. Arsenic incorporation into FeS2 pyrite and its influence on dissolution: A DFT study. Geochimica et Cosmochimica Acta, Vol. 71(3), p. 624-630

Bradbury, M.H. and B. Baeyens, 2005. Modelling the sorption of Mn(II), Co(II), Ni(II), Zn(II), Cd(II), Eu(III), Am(III), Sn(IV), Th(IV), Np(V) and U(VI) on montmorillonite: Linear free energy relationships and estimates of surface binding constants for some selected heavy metals and actinides. Geochimica et Cosmochimica Acta, 69(4), 875-892.

Bradl, H.B., 2004. Adsorption of heavy metal ions on soils and soils trace elements. Journal of Colloid and Interface Science, 277, 1-18.

Brantley, S.L. and M.A. Velbel, 1993. Preface to a special issue entitled "Geochemical kinetics of mineral-water reactions in the field and the laboratory". Chemical Geology, 105(1-3), vii-ix.

Carroll, S., Y. Hao, and R. Aines (2008), Transport and detection of carbon dioxide in dilute aquifers, 9th International Conference on Greenhouse Gas Control Technologies, November 2008, Washington, D.C., Energy Procedia.

Dixit, S. and J.G. Hering, 2003. Comparison of Arsenic(V) and Arsenic(III) Sorption onto Iron Oxide Minerals: Implications for Arsenic Mobility. Environmental Science & Technology, 37, 4182-4189.

Dzombak, D.A. and F.M.M. Morel, 1990. surface complexation modeling-hydrous ferric oxide. John wiley & sons, New York, 393 pp.

Rimstidt, J.D. and Vaughan, D.J., 2003. Pyrite oxidation: A state-of-the-art assessment of the reaction mechanism. Geochimica et Cosmochimica Acta, Vol. 67(5), pp. 873–880.

Goldberg, S., 2002. Competitive Adsorption of Arsenate and Arsenite on Oxides and Clay Minerals. SOIL SCI. SOC. AM. J., 66, 413-421.

Goldberg, S., S.M. Lesch, D.L. Suarez and N.T. Basta, 2005. Predicting Arsenate Adsorption by Soils using Soil Chemical Parameters in the Constant Capacitance Model. SOIL SCIENCE SOCIETY OF AMERICA JOURNAL 69(5), 1389-1398.Gu, X. and L.J. Evans, 2007. Modelling the adsorption of Cd(II), Cu(II), Ni(II), Pb(II), and Zn(II) onto Fithian illite. Journal of Colloid and Interface Science, 307, 317-325.

Henke, K., 2009. Arsenic: Environmental Chemistry, Health Threats and Waste Treatment. Wiley, 588 p.Hizal, J. and R. Apak, 2006. Modeling of copper(II) and lead(II) adsorption on kaolinite-based clay minerals individually and in the presence of humic acid. Journal of Colloid and Interface Science, 295, 1-13.

Hsieh, Y.H. and C. P. Huang, C.P., 1989. The Dissolution of PbS(s) in Dilute Aqueous Solutions *Journal of Colloid and Interface Science,* Vol, 131(2), p. 537-549.

Kharaka, Y., J. Thordsen, E. Kakouros, J. Birkholzer, J. Apps, L. Zheng, R. Trautz, H. Rauch, and K. Gullickson (2008): Changes in shallow groundwater chemistry following CO_2 injection at the ZERT field site, Bozeman, Montana, Proceedings AGU Fall Meeting 2008, San Francisco, CA, December, 2008.

Lackovic, K., M.J. Angove, J.D. Wells and B.B. Johnson, 2003. Modeling the adsorption of Cd(II) onto Muloorina illite and related clay minerals. Journal of Colloid and

Interface Science, 257, 31-40.Lasaga, A.C. 1998. Kinetic Theory in the Earth Sciences. Princeton University Press, Princeton, New Jersey. 811 p.

Lasaga, A.C. 1998. Kinetic Theory in the Earth Sciences. Princeton University Press, Princeton, New Jersey. 811 p.

Lasaga, A.C., and A. Luttge. 2001. Variation of crystal dissolution rate based on a dissolution stepwave model. Science (Washington, DC) 291:2400-2404.

Lasaga, A.C. and A. Luttge. 2003. A model for crystal dissolution. Eur. J. Mineral. 15:603-615.

Lasaga, A.C., J.M. Soler, J. Ganor, T.E. Burch and K.L. Nagy, 1994. Chemical weathering rate laws and global geochemical cycles. Geochimica et Cosmochimica Acta, 58, 2361-2368.

Luttge, A., 2006. Crystal dissolution kinetics and Gibbs free energy. Journal of Electron Spectroscopy and Related Phenomena, Vol. 150, p. 248–259

Lutzenkirchen, J., 2006. surface complexation modelling. Academic Press, Amsterdam, London, 638p pp.

Manning, B.A. and S. Goldberg, 1997. Adsorption and Stability of Arsenic(III) at the Clay Mineral-Water Interface. Environmental Science & Technology, 31: 2005-2011.

Matschullat, J., 2000. Arsenic in the geosphere - a review. The Science of the Total Environment, Vol. 249, p. 297-312.

McGrath, A.E., G.L. Upson, and M.D. Caldwell (2007), Evaluation and mitigation of landfill gas impacts on cadmium leaching from native soils, Ground Water Monitoring & Remediation, 27, 99–109.

McKibben, M.A., B.A. Tallant and J.K.d. Angel, 2008. Kinetics of inorganic arsenopyrite oxidation in acidic aqueous solutions. Applied Geochemistry, 23, 121-135.

Muller, B. and L. Sigg, 1991. Adsorption of Lead(ll) on the Goethite Surface: Voltammetric Evaluation of Surface Complexation Parameters. Journal of Colloid and Interface Science, 148(2), 517-532.

Nicholson, R. V., Gillham, R. W., and Reardon, E. J., 1990. Pyrite oxidation in carbonate-buffered solution: 2. Rate control by oxide coatings. Geochimica et Cosmochimica Acta, v. 54, p. 395-402.

Palandri, J. and Y.K. Kharaka, 2004. A compilation of rate parameters of water-mineral interaction kinetics for application to geochemical modeling. Open File Report 2004-1068, US Goelogical Survey.

Parkhurst, D.L. and C.A.J. Appelo, 1999. user's guide to PHREEQC (version 2)—a computer program for speciation, batch-reaction, one-dimensional transport, and inverse geochemical calculations. U.S. Geological Survey water-Resources Investigations Report 99-4259, Denver, Corolado.

Pitts, L.C. and Wallace, G.T. 1994: Lead deposition in the shell of the bivalve *Mya arenaria*: an indicator of dissolved lead in seawater. Estuarine, Coastal and Shelf Science, Vol. 39, p. 93–104.

Pokrovski, G.S., S. Kara and J. Roux, 2002. Stability and solubility of arsenopyrite, FeAsS, in crustal fluids. Geochim. et Cosmochim. Acta, 66(13), 2361–2378.Pruess, K., 2005. ECO2N: A TOUGH2 fluid property module for mixtures of water, NaCl and CO_2. LBNL-57592, Lawrence Berkeley National Laboratory.

Pruess, K., C. Oldenburg and G. Moridis, 1999. TOUGH2 User's Guide, Version 2.0. LBL-43134, Lawrence Berkeley National Laboratory, Berkeley, CA.

Reich, M. and U. Becker, 2006. First-principles calculations of the thermodynamic mixing properties of arsenic incorporation into pyrite and marcasite. Chemical Geology, 225, 278–290.

Reimer, R.A. and Miyazaki, A. , 1992. Determination of lead in sea-water by inductively coupled plasma atomic emission spectrometry combined with chelating resin preconcentration and hydride generation. Journal of Analytical Atomic Spectrometry, Vol. 7, p. 1239-1242.

Robie, R.A. and B.S. Hemingway, 1995. Thermodynamic properties of minerals and related substances at 298.15 K and 1 bar (105 pascals) pressure and at higher temperatures. Bull. 2131, U.S. Geol. Surv.

Román-Ross, G., Cuello, G.J., X. Turrillas, X., Fernández-Martínez, A. and Charle, L., 2006. Arsenite sorption and co-precipitation with calcite. Chemical Geology, vol. 233, 328–336.

Rozan, T.F., G.W.I. Luther, D. Ridge and S. Robinson, 2003. Determination of Pb complexation in oxic and sulfidic waters using pseudovoltammetry. Environmental Science & Technology., 37, 3845-3852.

Selim, H.M. and M.C. Amacher, 1996. Reactivity and transport of heavy metal in soil. Lewis Publishers, 201 pp.

Sonnenthal, E., A. Ito, N. Spycher, M. Yui, J. Apps, Y. Sugita, M. Conrad and S. Kawakami, 2005. Approaches to modeling coupled thermal, hydrological, and chemical processes in the Drift Scale Heater Test at Yucca Mountain. Int. J. Rock Mech. Min. Sci., 42, 6987–719.

Steefel, C.I., 2001. GIMRT, Version 1.2: Software for Modeling Multicomponent, Multidimensional Reactive Transport. Users Guide., Lawrence Livermore National Laboratory, Livermore, California.

Steefel, C.I. and A.C. Lasaga, 1994. A coupled model for transport of multiple chemical species and kinetic precipitation/dissolution reactions with applications to reactive flow in single phase hydrothermal system. Am. J. Sci, 294, 529–592.

Smyth, R.C., S.D. Hovorka, J. Lu, K.D. Romanak, J.W. Partin, and C. Wong (2008), Assessing risk to fresh water resources from long term CO_2 injection – laboratory and field studies, 9th International Conference on Greenhouse Gas Control Technologies, November 2008, Washington, D.C., Energy Procedia.

Utsunomiya, S., S.C. Peters, J.D. Blum, and R.C. Ewing, 2003, Nanoscale mineralogy of arsenic in a region of New Hampshire with elevated As-concentrations in the groundwater. Am. Miner. 88, 1844–1852.

Walker, F.P., M.E. Schreiber and J.D. Rimstidt, 2006. Kinetics of arsenopyrite oxidative dissolution by oxygen. Geochimica et Cosmochimica Acta, 70, 1668-1676.

Wang, S. and P.R. Jaffe, 2004. Dissolution of a mineral phase in potable aquifers due to CO_2 releases from deep formations; effect of dissolution kinetics. Energy Conversion and Management, 45, 2833-2848.

White, C.M., D.H. Smith, K.L. Jones, A.L. Goodman, R.B. LaCount, S.B. DuBose, E. zdemir, B.I. Morsi and K.T. Schroeder, 2005. Sequestration of carbon dioxide in coal with enhanced coalbed methane recovery—A review. Energy Fuels, 19, 659–724.

Wolery, T.J., 1993. EQ3/6, A software package for geochemical modelling of aqueous systems (Version 7.2). UCRL-MA 110662, Lawrence Livermore National Laboratory.

Wolthers, M., Butler, I.B., Rickard, D., Mason, P.R.D., 2005. Arsenic incorporation into p rite at ambient environmental conditions: a continuous-flow experiment. In: O'Day, P., Vlassopoulos, D., Meng, X., Benning, L. (Eds.), Advances in Arsenic Research: Integration of Experimental and Observational Studies and Implications for Mitigation, ACS Symposium Series, vol. 915. American Chemical Society, Washington, DC, pp. 60–76 (Chapter 5).

Xu, T., J.A. Apps, K. Pruess and H. Yamamoto, 2007. Numerical modeling of injection and mineral trapping of CO2 with H_2S and SO_2 in a sandstone formation. Chemical Geology, 242, 319-346.

Xu, T., E. Sonnenthal, N. Spycher and K. Pruess, 2005. TOUGHREACT User's Guide:A Simulation Program for Non-isothermal Multiphase Reactive Geochemical Transport in Variably Saturated Geologic Media. LBNL-55460, Ernest Orlando Lawrence Berkeley National Laboratory.

Xu, T., E. Sonnenthal, N. Spycher and K. Pruess, 2006. TOUGHREACT: A Simulation Program for Non-isothermal Multiphase Reactive Geochemical Transport in Variably Saturated Geologic Media. Computers and Geosciences, 32, 145-165.

Yu, Y., Y. Zhu, Z. Gao, C.H. Gammons and D. Li, 2007. Rates of Arsenopyrite Oxidation by Oxygen and Fe(III) at pH 1.8-12.6 and 15-45 °C. Environmental Science & Technology, 41, 6460-6464.

Zhang, S., J. Li, Y. Wang and G. Hu, 2004. Dissolution kinetics of galena in acid NaCl solutions at 25—75 ^{o}C. Applied Geochemistry, 19, 835-841.

Zhu, C. and Lu, P., 2009. Alkali feldspar dissolution and secondary mineral precipitation in batch systems: 3. Saturation states of product minerals and reaction paths. Geochimica et Cosmochimica Acta, 73(11), 3171-3200.

Zhu C., Blum A. E. and Veblen D. R. (2004a) Feldspar dissolution rates and clay precipitation in the Navajo aquifer at Black Mesa, Arizona, USA. In Water–Rock Interaction (eds. R. B. Wanty and R. R. I. Seal). A.A. Balkema, Saratoga Springs, New York, pp. 895–899.

Zhu C., Blum A. E. and Veblen D. R. D. (2004b) A new hypothesis for the slow feldspar dissolution in groundwater aquifers. Geochim. Cosmochim. Acta 68, A148.

Figures Captions

Figure 1. A schematic representation for the setup of reactive transport model.

Figure 2. Spatial distribution of total inorganic carbon (TIC) after 100 years of CO_2 intrusion

Figure 3. pH profiles along the x-axis at y = 0 m at different times.

Figure 4. Surface complex of lead on the strong site (a) and weak site (b) of illite along x-axis at y = 0 m at different times.

Figure 5. Relative change of total lead surface complexes concentration profiles along the x-axis at y = 0 m after 100 years of CO_2 intrusion.

Figure 6. Galena volume fraction change profiles along the x-axis at y = 0 m at different times.

Figure 7. Total aqueous lead concentration profile along x-axis at y = 0 m at different times.

Figure 8. Relative change of total arsenic surface complexes concentration along the x-axis at y = 0 m.

Figure 9. Arsenopyrite volume fraction change (right) along the x-axis at y = 0 m at different times.

Figure 10. Total aqueous arsenic concentration profile along x-axis at y = 0 m.

Figure 13. Comparison of model results for total aqueous lead (a) and arsenic (b) concentration profile along x at y=0 after 100 years of CO_2 intrusion in the sensitivity run (without sorption) with base model (with sorption).

Figure 14. Comparison of model results for total aqueous lead (left) and arsenic (right) concentration profile along x at y=0 after 100 years of CO_2 intrusion in the sensitivity run (site density = 6×10^{-7} mol/m^2) with base model (site density = 2.3×10^{-6} mol/m^2).

Figure 15. Computed total aqueous lead concentration after 100 years of CO_2 intrusion in sensitivity runs with different rate constant (k).

Figure 16. Computed total aqueous arsenic concentration after 100 years of CO_2 intrusion in sensitivity runs with different rate constant (k).

Figure 11. Computed total adsorbed lead (a) and total aqueous lead (b) after 100 years of CO_2 intrusion in sensitivity run (logK galena = -13.97) and base model (logK galena = -14.4)

Figure 12. Computed aqueous arsenic concentration after 100 years of CO_2 intrusion in a sensitivity run (logK arsenopyrite = 37.43) and base model (logK arsenopyrite = 37.93)

Figure 17. Comparison of TIC concentration profile along x at y=0 after 100 years of CO_2 intrusion in the sensitivity run (CO_2 intrusion rate of 6×10^{-4} kg/s) with base model (CO_2 intrusion rate of 7.5×10^{-5} kg/s).

Figure 18. Comparison of lead (a) and arsenic (b) concentration profile along x at y=0 after 100 years of CO_2 intrusion in the sensitivity run (CO_2 intrusion rate of 6×10^{-4} kg/s) with base model (CO_2 intrusion rate of 7.5×10^{-5} kg/s).

Table 1. Modal mineralogy of aquifer host rocks used in reactive transport simulations

Mineral	Chemical composition	Volume fraction
Quartz	SiO_2	0.689
K-feldspar	$KAlSi_3O_8$	0.061
Oligoclase	$CaNa_4Al_6Si_{14}O_{40}$	0.099
Kaolinite	$\underline{Al_2Si_2O_5(OH)_4}$	0.017
Smectite-Ca	$Ca_{0.14}Mg_{0.26}Si_{3.97}Al_{1.77}O_{10}(OH)_2$	0.013
Illite	$K_{0.6}Mg_{0.25}Si_{3.5}Al_{2.3}O_{10}(OH)_2$	0.028
Chlorite	$Fe_{2.5}Mg_{2.5}Si_3Al_2O_{10}(OH)_8$	0.010
Kerogen-OS	$C_{64}H_{102}O_{40}S_{10}$	0.0026
Dolomite	$CaMg(CO_3)_2$	0.000
Calcite	$CaCO_3$	0.015
Goethite	FeOOH	0.06
Arsenian pyrite	$FeAs_{0.05}S_{1.95}$	0.0051
Galena	PbS	8×10^{-6}

Table 2. Aqueous complexes and their dissociation constants

Species	Logk (25°C)	Species	Logk (25°C)	Species	Logk (25°C)	Species	Logk (25°C)
OH^-	13.99	$MgHCO_3^+$	-1.03	$CH_4(aq)$	144.15	$Pb(HSe)_2(aq)$	-20.78
Al^{+3}	-22.88	$CO_2(aq)$	-6.34	$H_2(aq)$	46.11	$Pb(HSe)_3$-	-22.17
$HAlO_2(aq)$	-6.45	CO_3^{-2}	10.33	$SO_2(aq)$	37.57	PbS(aq)	-5.5
$NaAlO_2(aq)$	0.75	$CaCO_3(aq)$	7.01	HSO_3^-	39.42	PbSe(aq)	-11.05

$AlOH^{+2}$	-17.87	KCl(aq)	1.50	$Pb(HS)_2(aq)$	-14.08	$H_2AsO_3^-$	9.13
$Al(OH)_2^+$	-12.78	$MgCl^+$	0.14	$Pb(HS)_3^-$	-15.30	$H_2AsO_4^-$	-21.41
$Al(OH)_3(aq)$	-6.72	$MgSO_4(aq)$	-2.38	$PbCl^+$	-1.45	$H_3AsO_4(aq)$	-23.64
$CaCl^+$	0.70	$NaSO_4^-$	-0.81	$PbCl_2(aq)$	-2.01	$HAsO_4^{-2}$	-14.66
$CaCl_2(aq)$	0.65	KSO_4^-	-0.88	$PbCl_3^-$	-1.70	$H_3As_3S_6(aq)$	-76.37
$CaSO_4(aq)$	-2.10	$NaHSiO_3(aq)$	8.30	$PbCl_4^{-2}$	-1.50	$H_2As_3S_6^-$	-72.79
NaCl(aq)	0.78	$CaOH^+$	12.85	$PbOH^+$	7.57	$HAs_3S_6^{-2}$	-64.88
$FeCl^+$	0.17	NaOH(aq)	14.15	$Pb(OH)_2(aq)$	17.07	$H_3As_3Se_6(aq)$	-83.42
$FeHCO_3^+$	-2.04	$NaCO_3^-$	9.82	$Pb(OH)_3^-$	28.07	$H_2As_3Se_6^-$	-79.36
$FeCO_3(aq)$	4.88	$H_3SiO_4^-$	9.81	$Pb(CO_3)_2^{-2}$	11.24	$HAs_3Se_6^{-2}$	-70.37
$FeCl_4^{-2}$	1.94	Fe^{+3}	-8.49	PbO(aq)	16.98	$HAsS_2(aq)$	-21.31
$NaHCO_3(aq)$	-0.17	FeS(aq)	2.20	$PbHCO_3^+$	-2.89	$AsSe(OH)(HSe)^-$	-26.88
$CaHCO_3^+$	-1.04	$H_2s(aq)$	-6.98	$PbCO_3(aq)$	-3.06	$AsS(OH)(HS)^-$	-21.83

Table 3. Solubility product of minerals

Primary Mineral	Solubility product	Primary Mineral	Solubility product	Secondary Mineral	Solubility product
Quartz	-3.75	Kerogen-os	72.76	Dolomite	5.76
K-feldspar	-22.91	Calcite	1.85	Magnesite	2.29
Oligoclase	-97.78	Goethite	-8.12	Ankerite	2.08
Kaolinite	-39.82	Arsenian pyrite	-21.7	Dawsonite	-18.53
Smectite-ca	-39.51	Galena	-14.4	Na-smectite	-39.53
Illite	-47.33			Pyromorphite	-63.29
Chlorite	4.29			Ferroselite	-56.9

Table 4. Kinetic properties for minerals considered in the model.

Mineral	**A**	**Parameters for Kinetic Rate Law**		
	(cm^2/g)	**Neutral Mechanism**	**Acid Mechanism**	**Base Mechanism**

		k_{25} (mol/m^2/s)	E_a (KJ /mol)	k_{25}	E_a	n(H^+)	k_{25}	E_a	n(H^+)
***Primary*:**									
Quartz	9.8	1.023×10^{-14}	87.7						
K-feldspar	9.8	3.89×10^{-13}	38	8.71×10^{-11}	51.7	0.5	6.31×10^{-12}	94.1	-0.823
Oligoclase	9.8	1.44×10^{-12}	69.8	2.13×10^{-10}	65	0.457			
Kaolinite	1.95×10^{5}	6.91×10^{-14}	22.2	4.89×10^{-12}	65.9	0.777	8.91×10^{-18}	17.9	-0.472
Smectite-Ca	5.64×10^{5}	1.66×10^{-13}	35	1.05×10^{-11}	23.6	0.34	3.02×10^{-17}	58.9	-0.4
Illite	6.68×10^{5}	1.66×10^{-13}	35	1.05×10^{-11}	23.6	0.34	3.02×10^{-17}	58.9	-0.4
Chlorite	9.8	3.02×10^{-13}	88	7.76×10^{-12}	88	0.5			
Kerogen-os	9.8	3.02×10^{-13}	88	7.76×10^{-12}	88	0.5			
Calcite	Assumed at equilibrium								
Goethite	1.47×10^{5}	2.52×10^{-12}	62.76						
Arsenian pyrite	12.9	2.52×10^{-12}	62.76						
Galena	12.9			2.34×10^{-7}	43.54	1			
Secondary:									
Dolomite	12.9	2.52×10^{-12}	62.76	2.34×10^{-7}	43.54	1			
Magnesite	9.8	4.57×10^{-10}	23.5	4.17×10^{-7}	14.4	1			
Ankerite	9.8	1.26×10^{-9}	62.76	6.46×10^{-4}	36.1	0.5			
Dawsonite	9.8	1.26×10^{-9}	62.76	6.46×10^{-4}	36.1	0.5			
Smectite-Na	5.64×10^{5}	1.66×10^{-13}	35	1.05×10^{-11}	23.6	0.34	3.02×10^{-17}	58.9	-0.4
Pyromorphite	12.9	2.52×10^{-12}	62.76	2.34×10^{-7}	43.54	1			
Ferroselite	12.9	2.52×10^{-12}	62.76	2.34×10^{-7}	43.54	1			

Table 5. Surface complexation of lead on different minerals.

Adsorbent	Surface Complexes	Reactions	Log k_{int}	Reference
goethite	Goe_OPb^+	Goe _$OPb^+ + H^+$ □ Goe_OH + Pb^{+2}	0.5	(Muller and Sigg, 1991)
goethite	(Goe _$O)_2Pb$	(Goe _$O)_2Pb+2H^+$ □ 2Goe_OH + Pb^{+2}	6.24	
kaolinite	Kao_OPb^+	Kao_$OPb^+ + H^+$ □ Kao_OH + Pb^{+2}	-1.89	(Hizal and Apak, 2006)
illite	Ill^s_OPb^+	Ill^s_$OPb^+ + H^+$ □ Ill^s_OH + Pb^{+2}	-1.37	(Gu and Evans, 2007)
illite	Ill^w_OPb^+	Ill^w_$OPb^+ + H^+$ □ Ill^w_OH + Pb^{+2}	3.84	
smectite	Sme^s_OPb^+	Sme^s_$OPb^+ + H^+$ □ Sme^s_OH + Pb^{+2}	-1.12	(Bradbury and Baeyens, 2005)
smectite	Sme^w_OPb^+	Sme^w_$OPb^+ + H^+$ □ Sme^w_OH + Pb^{+2}	1.28	

Table 6. Surface complexation of arsenic on different minerals

Adsorbent	Surface Complexes	Reactions	Log k_{int}	Reference

goethite	Goe $\_H_2AsO_3$	Goe $\_H_2AsO_3 + H_2O$ ⇌ Goe $\_OH + H_3AsO_3$	-5.19	(Dixit and
goethite	Goe $\_HAsO_3^-$	Goe $\_HAsO_3^- + H_2O + H^+$ ⇌ Goe$_OH + H_3AsO_3$	2.34	Hering, 2003)
kaolinite	Kao$_H_2AsO_3$	Kao $\_H_2AsO_3 + H_2O$ ⇌ Kao $\_OH + H_3AsO_3$	-8.23	(Manning and
kaolinite	Kao $\_HAsO_3^-$	Kao$_HAsO_3^- + H_2O + H^+$ ⇌ Kao $\_OH + H_3AsO_3$	0.664	Goldberg,
kaolinite	Kao $\_OAsO_3^{2-}$	Kao$_AsO_3^{2-} + H_2O + 2H^+$ ⇌ Kao $\_OH + H_3AsO_3$	13.67	1997)
illite	Ill$_H_2AsO_3$	Ill $\_H_2AsO_3 + H_2O$ ⇌ Ill$_OH + H_3AsO_3$	-9.07	(Manning and
illite	Ill $\_HAsO_3^-$	Ill $\_HAsO_3^- + H_2O + H^+$ ⇌ Ill $\_OH + H_3AsO_3$	-3.0	Goldberg,
illite	Ill$_AsO_3^{2-}$	Ill$_AsO_3^{2-} + H_2O + 2H^+$ ⇌ Ill$_OH + H_3AsO_3$	10.3	1997)
smectite	Sme $\_H_2AsO_3$	Sme $\_H_2AsO_3 + H_2O$ ⇌ Sme $\_OH + H_3AsO_3$	-8.89	(Manning and
smectite	Sme $\_HAsO_3^-$	Sme $\_HAsO_3^- + H_2O + H^+$ ⇌ Sme $\_OH + H_3AsO_3$	4.65	Goldberg,
smectite	Sme $\_AsO_3^{2-}$	Sme $\_AsO_3^{2-} + H_2O + 2H^+$ ⇌ Sme $\_OH + H_3AsO_3$	13.7	1997)

Table 7. Specific surface area and site densities used in the base model

Absorbent	**Specific surface area (cm^2/g)**	**Site density (mol/m^2)**		**Reference**
		Strong site	**Weak site**	
goethite	1.47×10^5	1.76×10^{-6}	3.22×10^{-6}	(Muller and Sigg, 1991)
kaolinite	1.95×10^5	2.2×10^{-6}	3.0×10^{-6}	(Lackovic et al., 2003)
illite	6.68×10^5	1.3×10^{-6}	2.27×10^{-6}	(Gu and Evans, 2007)
smectite	5.64×10^5	4.77×10^{-8}	9.54×10^{-7}	(Bradbury and Baeyens, 2005)

Table 8. Hydrodynamic parameters

Porosity	0.3

Intrinsic permeability	1×10^{-12} m^2 (hydraulic conductivity of ≈ 0.86 m/day)
Relative permeability (van Genuchten-Mualem model)	$k_{rl} = \sqrt{S^*}\left\{1-\left(1-\left[S^*\right]^{1/0.457}\right)^{0.457}\right\}^2$ with $S^* = (S_l - 0.3)/(1.0-0.3)$ where S_l is the liquid saturation degree
Gas relative permeability	$k_{rg} = \left(1-\hat{S}\right)^2\left(1-\hat{S}^2\right)$ with $\hat{S} = \left(S_l - 0.3\right)/\left(1-0.3-0.05\right)$
Capillary pressure function	$P_{cap} = -\frac{1}{5.1\times10^{-5}}\left(\left[S^*\right]^{-1/0.457}-1\right)^{1-0.457}$ with $S^* = S_l / 0.999$ and subject to restriction $-10^7 \le P_{cap} \le 0$
Molecular diffusion coefficient	10^{-9} m^2/s

Table 9. Initial total aqueous concentration of major constituents obtained by initial equilibrium run for the base model.

Species	Concentration (mol/L)	Species	Concentration (mol/L)
Ca	9×10^{-4}	TIC	3.3×10^{-3}
Mg	2.2×10^{-5}	SO_4^{-2}	1.9×10^{-4}
Na	2×10^{-3}	Cl	2.1×10^{-4}
K	2.7×10^{-4}	Pb	1.3×10^{-9}
Fe	5.6×10^{-6}	As	4.4×10^{-8}
Si	9.3×10^{-4}	ionic strength	0.0051

Table 10. Mass distribution (mol % with respect to the total mass at t = 0) of Pb and As on solid (in mineral or adsorbed on mineral surfaces) and liquid phase at initial (t = 0) and final time (t = 100 years) after CO_2 intrusion at about 5 bar at the point of intrusion.

	aqueous phase	mineral	Adsorbed on goethite	Adsorbed on kaolinite	Adsorbed on illite	Adsorbed on smectite	Total adsorbed	total mass (mol/L)	time
Lead	0.0002	99.12	0.09	0.0002	0.79	0.004	0.89	100.000	t=0
Lead	0.0024	99.42	0.01	0.0004	0.09	0.017	0.11	99.532	t=100 year
arsenite	0.0001	37.1238	0.08	0.03	55.29	7.48	62.88	100.000	t=0
arsenite	0.0002	37.1237	0.10	0.03	55.13	7.62	62.87	99.997	t=100 year

Table 11. Concentration (in mol/L) of some lead aqueous species after initial equilibrium in base model and in the sensitivity run to solubility product of galena.

Species	**Base model**	**Sensitivity run**
PbS(aq)	1.11×10^{-9}	2.98×10^{-9}
PbSe(aq)	1.83×10^{-10}	1.78×10^{-10}
$PbCO_3$(aq)	1.77×10^{-11}	4.77×10^{-11}
Pb^{+2}	2×10^{-13}	5.5×10^{-13}
Total aqueous Pb	1.30×10^{-9}	3.21×10^{-9}
Total adsorbed Pb	5.09×10^{-6}	1.36×10^{-5}

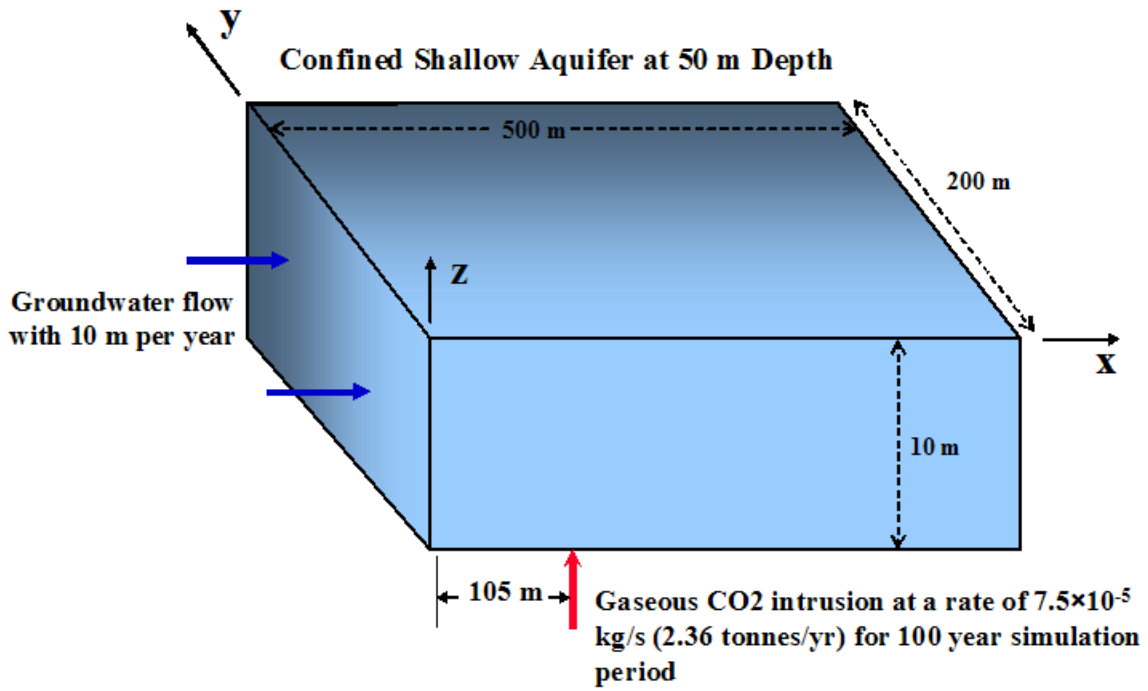

Figure 1.

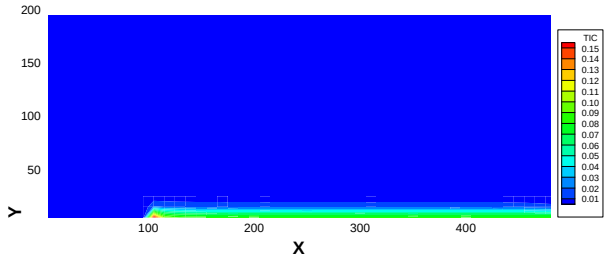

Figure 2.

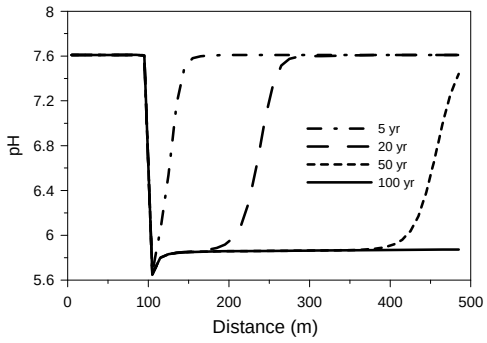

Figure 3.

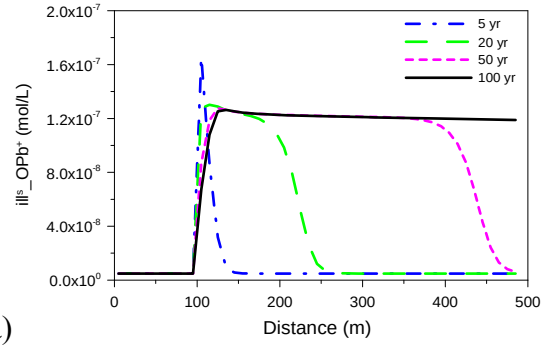

(a)

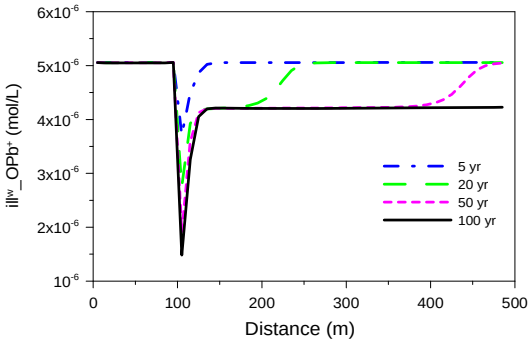

(b)

Figure 4.

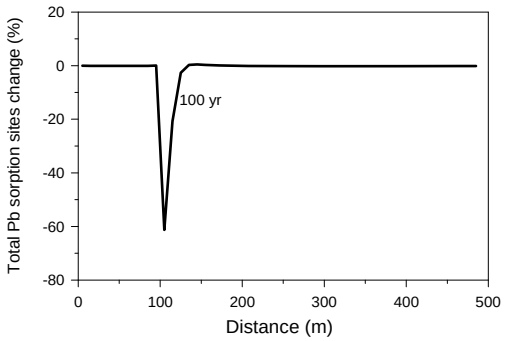

Figure 5.

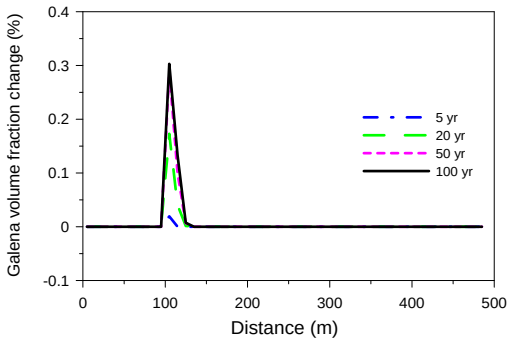

Figure 6.

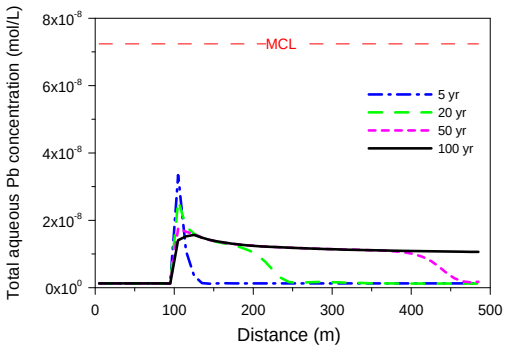

Figure 7.

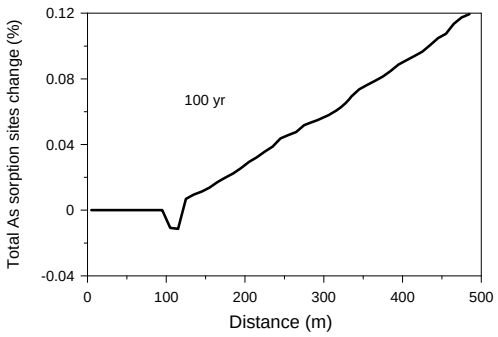

Figure 8.

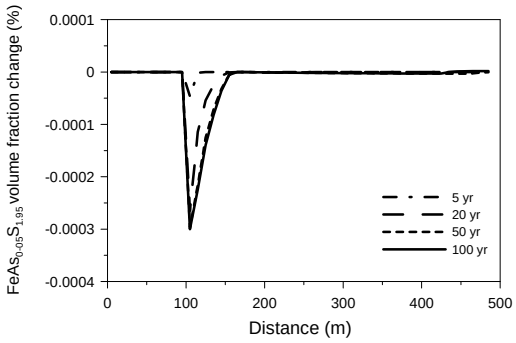

Figure 9.

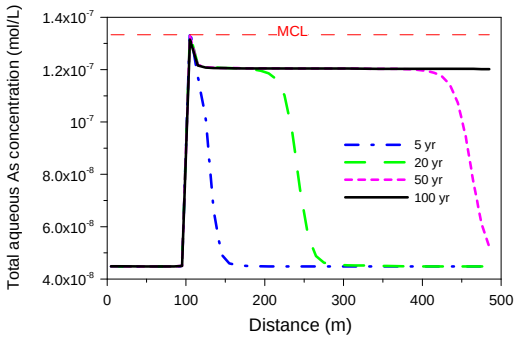

Figure 10.

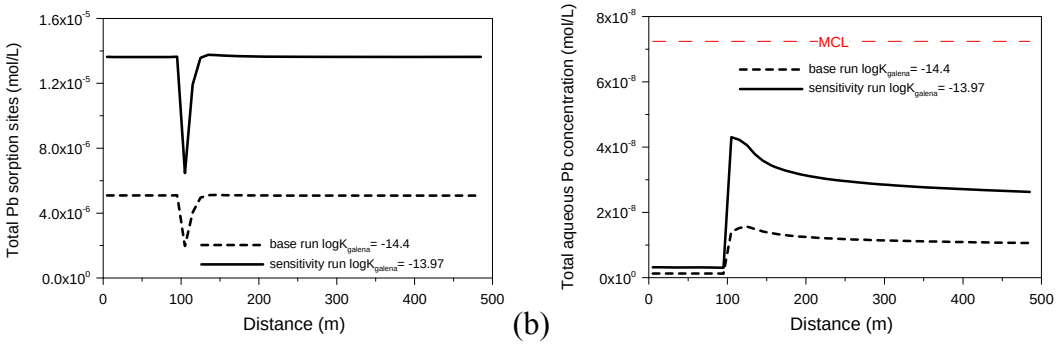

Figure 11.

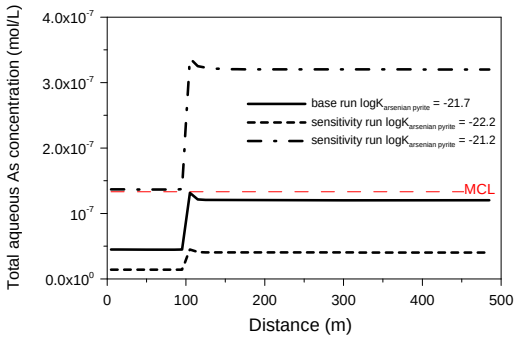

Figure 12.

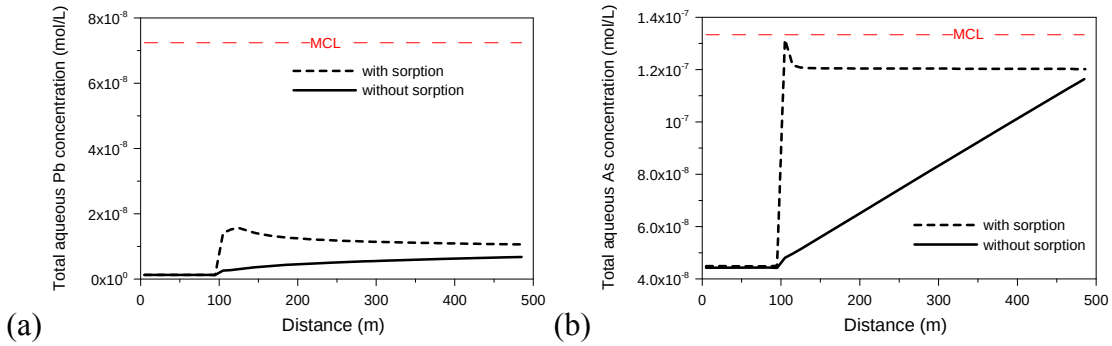

Figure 13.

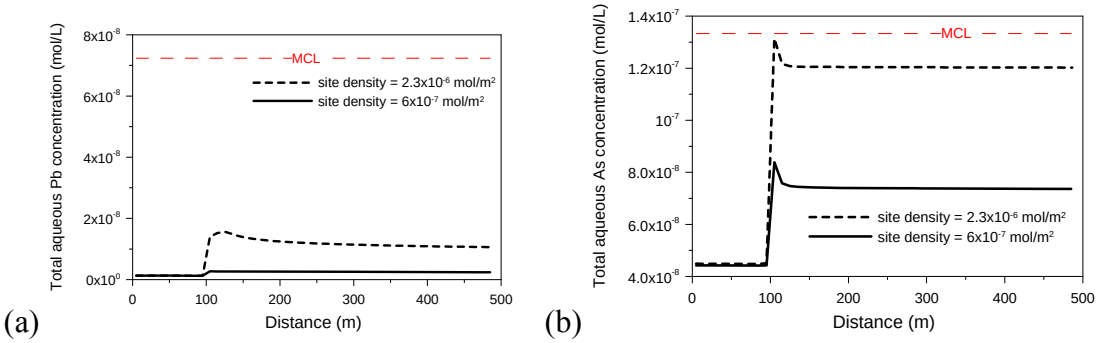

Figure 14.

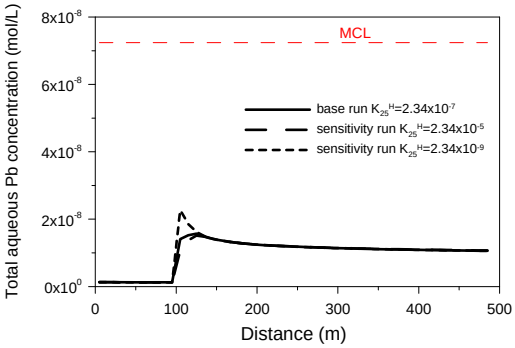

Figure 15.

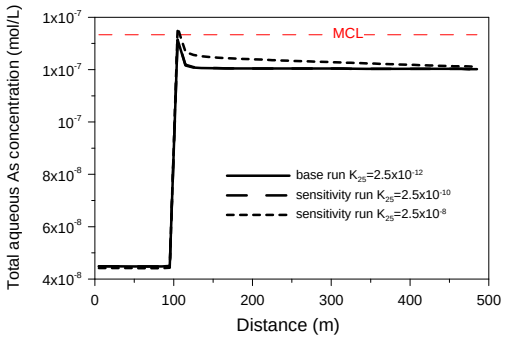

Figure 16.

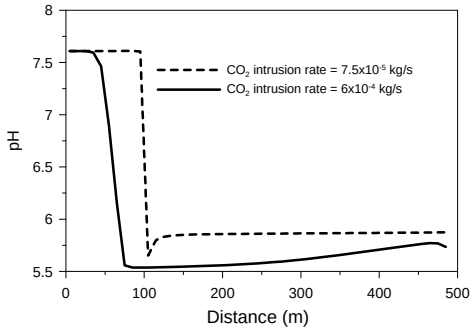

Figure 17.

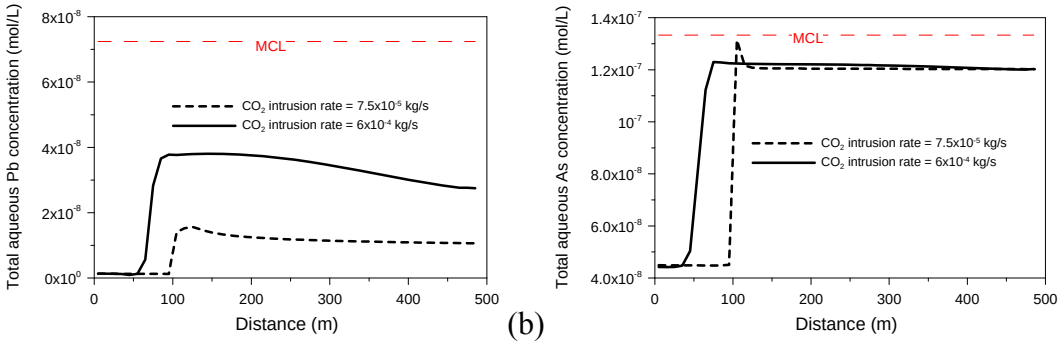

Figure 18.